Geosci. Model Dev. Discuss., 8, 5671–5739, 2015
www.geosci-model-dev-discuss.net/8/5671/2015/
doi:10.5194/gmdd-8-5671-2015

Geoscientific Model Development Discussions
Open Access

Development and evaluation of CNRM Earth-System model – CNRM-ESM1

R. Séférian[1], C. Delire[1], B. Decharme[1], A. Voldoire[1], D. Salas y Melia[1], M. Chevallier[1], D. Saint-Martin[1], O. Aumont[2], J.-C. Calvet[1], D. Carrer[1], H. Douville[1], L. Franchistéguy[1], E. Joetzjer[3], and S. Sénési[1]

[1]CNRM-GAME, Centre National de Recherches Météorologiques-Groupe d'Etude de l'Atmosphère Météorologique, Météo-France/CNRS, 42 Avenue Gaspard Coriolis, 31057 Toulouse, France
[2]Sorbonne Universités (UPMC, Univ Paris 06)-CNRS-IRD-MNHN, LOCEAN-IPSL Laboratory, 4 Place Jussieu, 75005 Paris, France
[3]Montana State University, Institute on Ecosystems, Department of Ecology, 111 AJM Johnson Hall, Bozeman, Montana 59717, USA

Received: 18 June 2015 – Accepted: 9 July 2015 – Published: 22 July 2015

Correspondence to: R. Séférian (roland.seferian@meteo.fr)

Published by Copernicus Publications on behalf of the European Geosciences Union.

Abstract

We introduce and document the first version of the Centre National de Recherches Météorologiques Earth system model (CNRM-ESM1). This model is based on the physical core of the CNRM-CM5 model and employs the Interactions between Soil, Biosphere and Atmosphere (ISBA) module and the Pelagic Interaction Scheme for Carbon and Ecosystem Studies (PISCES) as terrestrial and oceanic components of the global carbon cycle. We describe a preindustrial and 20th century climate simulation following the CMIP5 protocol. We detail how the various carbon reservoirs were initialized and analyze the behavior of the carbon cycle and its prominent physical drivers. CNRM-ESM1 reproduces satisfactorily several aspects of the modern carbon cycle. On land, the model reasonably captures the carbon cycling through vegetation and soil, resulting in a net terrestrial carbon sink of 2.2 $\mathrm{Pg\,C\,y^{-1}}$. In the ocean, the large-scale distribution of hydrodynamical and biogeochemical tracers agrees well with a modern climatology from the World Ocean Atlas. The combination of biological and physical processes induces a net CO_2 uptake of 1.7 $\mathrm{Pg\,C\,y^{-1}}$ that falls within the range of recent estimates. Our analysis shows that the atmospheric climate of CNRM-ESM1 compares well with that of CNRM-CM5. Biases in precipitation and shortwave radiation over the Tropics generate errors in gross primary productivity and ecosystem respiration. Compared to CNRM-CM5, the revised ocean–sea ice coupling has modified the sea-ice cover and ocean ventilation, unrealistically strengthening the flow of North Atlantic deep water (26.1 ± 2 Sv). It results in an accumulation of anthropogenic carbon in the deep ocean.

1 Introduction

Earth system models (ESMs) are now recognized as the current state-of-the-art models (IPCC, 2013), expanding the numerical representation of the climate system of the 4th Assessment Report (IPCC, 2007). They enable the representation of subtle non-linear interactions and feedbacks of different magnitude and signs of various bio-

GMDD
8, 5671–5739, 2015

geochemical and biophysical processes with the climate system. The latter contribute, in addition to the atmospheric radiative properties and global climate dynamics, to determine the Earth's climate variability (Arora et al., 2013; Cox et al., 2000; Friedlingstein and Prentice, 2010; Schwinger et al., 2014; Wetzel et al., 2006).

Although there is no uniformly accepted definition, ESMs generally bring together a global physical climate model and land and ocean biogeochemical modules (Bretherton, 1985). As such, they enable the representation of the global carbon cycle. The models of this class have played a larger role in the 5th IPCC report than in previous reports, primarily through their contribution to the concentration- and emission-driven experiments that compose CMIP5.

Even if the concept of Earth system modeling is being extended to include further processes and reservoirs (e.g., nitrogen cycle, aerosols) (Hajima et al., 2014), there are still large uncertainties in the representation of the carbon cycle and its interactions with climate (Anav et al., 2013a; Friedlingstein et al., 2013; Piao et al., 2013). To reduce them, there is a need for improvements of both physical and ecophysiological parameterizations (Dalmonech et al., 2014), and for the development of observation-based methods to constrain model projections (Wenzel et al., 2014). But the reduction of carbon cycle-climate uncertainties also requires a greater ensemble of ESMs. This path is promoted and followed by various international initiatives like the Global Carbon Budget (http://www.globalcarbonproject.org/) that sequentially incorporate more and more models into their analyses (Le Quéré et al., 2013, 2015).

This manuscript documents the first IPCC-class ESM developed at Centre National de Recherches Météorologiques and provides a basic evaluation of the model's skill. This model is based on the CNRM-CM5.1 climate model jointly developed by CNRM and Cerfacs (Centre Européen de Recherche et de Formation Avancée en Calcul Scientifique), which has contributed to the fifth phase of the Coupled Model Intercomparison Project (CMIP5) (Voldoire et al., 2013). CNRM-CM5.1 did not include a representation of the global carbon cycle but accounted for chemical-climate interactions with an interactive stratospheric chemistry module (Cariolle and Teyssedre,

GMDD
8, 5671–5739, 2015

2007). While this configuration of CNRM-CM5 contributed to the CMIP5 results publicly released, a first intermediate version of the CNRM ESM was developed with the inclusion of the marine biogeochemistry model PISCES (Aumont and Bopp, 2006). This model version was evaluated against modern oceanic observations (Séférian et al., 2013) and employed in various studies (Frölicher et al., 2014; Laufkötter et al., 2015; Schwinger et al., 2014; Séférian et al., 2014).

A terrestrial carbon cycle module is being developed at CNRM since the 2000s (Calvet and Soussana, 2001; Calvet et al., 2008, 2004; Gibelin et al., 2008, 2006), but it has never been coupled to an atmosphere–ocean model. This carbon cycle module evolved from the physically-based ISBA model (Noilhan and Mahfouf, 1996; Noilhan and Planton, 1989) and is able to simulate the surface carbon fluxes and the terrestrial carbon pools. The carbon fluxes module was extensively tested over France and Europe (Sarrat et al., 2007; Szczypta et al., 2012), and the carbon cycle module was tested for temperate and high latitude regions (Gibelin et al., 2006, 2008) and was used more recently in studies of carbon cycling over the Amazon basin (Joetzjer et al., 2015, 2014), permafrost regions (Rawlins et al., 2015) and at global scale (Carrer et al., 2013b). In this work, this terrestrial carbon cycle module is coupled to a global climate model for the first time.

Here, we present a first evaluation of the CNRM-ESM1. In Sect. 2, we describe the model, focusing on the Earth system's components and aspects of the climate model that are particularly relevant to the global carbon cycle. We describe in Sect. 3 the pre-industrial control and 20th century experiments that we conducted, together with the forcings used and how the experiments were initialized. In Sect. 4, we present and discuss the results of these experiments. We summarize the results in Sect. 5 and present conclusions.

GMDD
8, 5671–5739, 2015

2 CNRM-ESM components

2.1 The physical core

CNRM-ESM1 is based on the physical core of the CNRM-CM5.1 AOGCM model extensively described in Voldoire et al. (2013), which accounts for the physical and dynamical interactions occurring between atmosphere, land, ocean and sea-ice (ARPEGE-Climat, SURFEX, NEMO, GELATO, respectively).

The atmospheric component is based on version 6.1 of the global spectral model ARPEGE-Climat whereas CNRM-CM5.1 was based on version 5.2. This version of the atmospheric code derives from cycle 37 of the ARPEGE-IFS (Integrated Forecast System) numerical weather prediction model developed jointly by Météo-France and the European Center for Medium-range Weather Forecast. In CNRM-ESM1, the geometry, parameterizations and dynamics have been chosen to match the choices made for CNRM-CM5.1. Thus differences are mainly due to debugging and recoding. The atmospheric physics and dynamics are solved on a T127 triangular truncation that offers a spatial resolution of about 1.4° in both longitude and latitude. Consistently to CNRM-CM5.1, CNRM-ESM1 employs a "low-top" configuration with 31 vertical levels that extend from the surface to 10 hPa in the stratosphere. The layers are unevenly distributed with 6 layers below 850 hPa except in regions of high orography, nine layers above 200 hPa and four layers above 100 hPa. The dynamical core of the model, the radiative scheme for longwave and shortwave as well as the physical parameterization for deep and shallow convection are identical to those employed in CNRM-CM5.1. The reader is referred to Voldoire et al. (2013) for the original description of the atmospheric model parameterizations. The main difference from the CNRM-CM5.1 atmospheric model is the improved treatment of volcanic aerosols.

The land-surface component is an updated version of the SURFface EXternalisée modeling platform (SURFEXv7.3) (Masson et al., 2013b) associated with the Total Runoff Integrating Pathways (TRIP) river routing model (Oki and Sud, 1997). SURFEX was designed so that the same code could be run offline or coupled to a GCM, to

GMDD
8, 5671–5739, 2015

allow easy transfer from offline improvements to the coupled model and to be able to compare online and offline runs.

This model prognostically computes the exchange of energy, water and carbon between the atmosphere and three types of natural surfaces: land, free water bodies, oceans or seas. The energy, water and carbon balances are calculated separately for each surface type and area-averaged over each atmospheric grid cell. The natural land surfaces are represented by the module originally developed by Noilhan and Planton (1989). This module solves the surface energy and soil water budgets using the force-restore method and a composite soil-vegetation-snow approach. The version used here is the same as for CNRM-CM5.1; e.g. the soil hydrology uses 3 vertical layers (Boone et al., 1999) while soil temperature is solved using 4 vertical layers. In CNRM-ESM1, land surface albedo benefits from an improved spatial representation derived from MODIS satellite measurements (Carrer et al., 2013a) except for the area covered by snow for which the albedo is prognostically computed following Douville et al. (1995). Over water bodies and oceans, we use the CNRM-CM5.1 parameterization for momentum and energy fluxes except for the sea-to-air turbulent fluxes that are computed from the COARE scheme (Fairall et al., 2003). Interactions between the land surface energy and water budgets and the terrestrial carbon cycle module are detailed in Sect. 2.3.1.

The ocean component uses version 3.2 of the NEMO model (Madec, 2008) in the ORCA1L42 configuration. This configuration offers a horizontal resolution from 1 to 1/3° near the equator and 42 levels in depth. The vertical discretization uses a partial-step formulation (Barnier et al., 2006), which ensures a better representation of bottom bathymetry and thus stream flow and friction at the bottom of the ocean. Ocean dynamics and physics is solved using a timestep of 1 h. Vertical physics relies on the parameterization chosen for the CNRM-CM5.1 climate model. The mixed layer dynamics is parameterized using a double diffusion process (Merryfield et al., 1999), Langmuir cell (Axell, 2002) and account for the contribution of surface wave breaking (Mellor and Blumberg, 2004). A parameterization of bottom intensified tidal-driven mixing similar to

GMDD
8, 5671–5739, 2015

Simmons et al. (2004) is used in combination with a specific tidal mixing parameterization in the Indonesian area (Koch-Larrouy et al., 2010, 2007). Finally, CNRM-ESM1 benefits from an improved Turbulent Kinetic Energy (TKE) closure scheme (Madec, 2008), based on the Blanke and Delecluse (1993) TKE. This parameterization allows a fraction of surface wind energy to penetrate below the base of the mixed layer ensuring a better coupling between surface wind and subsurface mixing. The main difference from the CNRM-CM5.1 ocean model is the explicit modulation of the radiative shortwave penetration into the ocean by marine biota (Lengaigne et al., 2009; Mignot et al., 2013), which is further detailed in Sect. 2.3.2.

The sea-ice model used in CNRM-ESM1 is GELATO6. This model employs the same horizontal grid as NEMO and solves sea-ice dynamics and thermodynamics every 6 h. This model represents an updated version of the former sea-ice model used in CNRM-CM5.1 (Voldoire et al., 2013). In GELATO6, sea-ice dynamics is computed using the Elastic–Viscous–Plastic scheme proposed by Hunke and Dukowicz (1997) formulated on an Arakawa C-grid (Bouillon et al., 2009). To simulate the response of sea ice to convergence-divergence movements, GELATO6 employs a redistribution scheme derived from Thorndike et al. (1975). This scheme ensures the representation of the rafting phenomenon for the slab of sea ice thinner than 0.25 m and of ridging for the slab thicker than 0.25 m. GELATO6 includes a thermodynamic scheme that resolves the evolution of four ice thickness categories (0–0.3, 0.3–0.8, 0.8–3 and over 3 m). These four slabs of sea ice are modeled with 10 vertical layers unevenly distributed across the slab thickness. An enhanced resolution at the top of the slab is used to better represent the evolution of sea ice in response to the high frequency variability of the atmospheric thermal forcing. Besides, all sea-ice slabs may be covered with one snow layer. In GELATO6, the snow layer is considered to occult the transfer of light across the snow–sea ice–ocean continuum. This snow layer can age or form ice using the formulation described in Salas y Mélia (2002). Since CNRM-CM5.1, the coupling between NEMO and GELATO has been revised in order to improve the conservation of water and salt.

GMDD
8, 5671–5739, 2015

The coupling between the atmosphere and the surface models is implicit and occurs every atmospheric timestep (i.e., 30 min) while the coupling between the atmosphere and the ocean models is handled by the OASIS coupler (Valcke, 2013) and occurs every 6 h. In CNRM-ESM1, the frequency of coupling between the ocean and atmosphere models has been increased compared to CNRM-CM5 in order to better resolve the dynamics of the sea-ice, which is resolved at this timestep (i.e., 6 h).

2.2 Atmospheric chemistry

The atmospheric chemistry scheme in CNRM-ESM1 consists of an interactive linear ozone chemistry model MOBIDIC (Cariolle and Teyssedre, 2007) including a representation of the three-dimensional atmospheric CO_2 mixing ratio.

As in CNRM-CM5, the ozone mixing ratio is treated as a prognostic variable with photochemical production and loss rates climatology computed by a full chemistry scheme. That is, the net photochemical production in the ozone continuity equation is solved using a first-order Taylor series around the local value of the ozone mixing ratio, air temperature, and the overhead ozone column. Ozone destruction terms are used to parameterize the heterogeneous chemistry as a function of the equivalent chlorine content prescribed for the actual year. All Taylor coefficients of this linearized scheme were determined using a two-dimensional chemistry scheme with 56 constituents, 175 chemical reactions, and 51 photoreactions (Cariolle and Brard, 1985). In this version, the gas-phase chemical rates were upgraded according to the recommendations of the JPL-2003-25 report (Sander et al., 2006). Photochemical production and loss rates of ozone rely on the main gas-phase reactions driving the NO_x, HO_x, ClO_x, BrO_x catalytic cycles. While the ozone mixing ratio is fully described across the atmospheric column, the linear ozone scheme was especially designed to resolve its evolution in the stratosphere for the sake of radiative transfer calculation. Therefore, some tropospheric chemical reactions are not taken into account in this scheme. The reader is referred to a manuscript by Eyring et al. (2013) for an extensive evaluation of the lin-

GMDD
8, 5671–5739, 2015

ear scheme vs. TOMS satellite measurements and intercomparison with other CMIP5 models.

In CNRM-ESM1, the atmospheric CO_2 mixing ratio can be treated as a prognostic tracer. It responds interactively to natural CO_2 exchange from land and ocean every 30 min and 6 h, respectively, while anthropogenic carbon emissions are prescribed in this model version. The CO_2 mixing ratio can affect the physical climate by impacting the atmospheric radiative transfer computations and both terrestrial and marine carbon uptake. In the present concentration-driven experiments, the CO_2 mixing ratio is however prescribed to the global yearly average atmospheric concentrations provided by CMIP5.

2.3 The biogeochemical components

2.3.1 Land biogeochemical model

In CNRM-ESM1, the interactions between climate and vegetation are handled by the ISBA scheme embedded in the SURFEX surface model. The land biogeochemical module in ISBA represents land surface physics, plant physiology, carbon allocation and turnover, and carbon cycling through litter and soil (Calvet and Soussana, 2001; Calvet et al., 1998; Gibelin et al., 2006, 2008). The land cover is represented by 9 plant functional types (PFT, given in Fig. 1) and 3 non-vegetated surfaces that are determined spatially by the ECOCLIMAP physiographic database (Masson et al., 2013a).

ISBA uses a semi-mechanistic treatment of canopy photosynthesis and mesophyll conductance following the Jacobs et al. (1996) and Goudriaan et al. (1985) photosynthesis model. Mesophyll conductance in this framework corresponds to the rate of photosynthesis under light-saturated conditions (Jacobs et al., 1996). As such, this scheme does not explicitly account for Michealis–Menten kinetics of the Rubisco enzyme found in Farquhar et al. (1980) and Collatz et al. (1992) models. ISBA includes a representation of the soil water stress. Key parameters of the photosynthesis model respond to the soil water stress, permitting the representation of drought-avoiding and

GMDD
8, 5671–5739, 2015

drought-tolerant responses to drought. For low vegetation and for trees, the response to drought is based on the meta-analyses of Calvet (2000) and Calvet et al. (2004) respectively.

The model simulates a ratio of intercellular CO_2 to atmospheric CO_2 that depends on leaf-to-air saturation deficit, leaf temperature, and soil moisture. Assimilation is calculated from this ratio, air CO_2 concentration, leaf temperature, and solar radiation considering plant photosynthetic pathways: C_3 or C_4 (Calvet et al., 1998; Gibelin et al., 2006). Stomatal conductance, which represents the vegetation control on gas transfer (here, CO_2 and water vapor) between the leaves and the atmosphere, is finally deduced from the assimilation rate. Leaf dark respiration is taken as a fraction of maximum CO_2 limited rate of assimilation. Standard Q_{10} response functions determine the temperature dependencies of mesophyll conductance, CO_2 compensation point, maximum photosynthetic rate and hence photosynthesis and respiration.

ISBA simulates the evolution of 6 reservoirs of biomass including leaf, wood, and roots, and assumes the existence of metabolic/structural reservoirs of biomass (Gibelin et al., 2008). Vegetation biomass is simulated interactively based on the carbon assimilated by photosynthesis, and decreased by turnover and respiration. The autotrophic respiration combines the respiration from all these reservoirs except the woody reservoir that is supposed not to respire (Gibelin et al., 2008). In this model, the vegetation phenology results directly from the carbon balance of the leaves. Therefore, phenology is completely driven by photosynthesis and no growing degree-day model is used. This is a key advantage of this approach as most the soil and atmospheric drivers (the abiotic drivers) of phenology are accounted for, without any additional parameters (Szczypta et al., 2014). Leaf area index (LAI) is determined from the leaf biomass and the specific leaf area ratio, which varies as a function of leaf nitrogen concentration and plant functional type (Gibelin et al., 2006). An implicit nitrogen limitation model is implemented in ISBA growth model (Calvet et al., 2008). This simple implicit nitrogen limitation is used to relate internal concentration of nitrogen to biomass and to limit the net assimilation of atmospheric CO_2.

GMDD
8, 5671–5739, 2015

The soil organic matter and litter module in ISBA follows the soil carbon part of the CENTURY model (Parton et al., 1988). Four pools of litter are represented. They are differentiated by their location above- or below-ground and their content of lignin. The litter pools are supplied by the fluxes of dead biomass from each biomass reservoir (turnover) as described in Gibelin et al. (2008). The 3 soil organic matter reservoirs (active, slow and passive) are characterized by their resistance to decomposition with turnover times spanning from a few months for the active pool to 240 years for the passive pool. Heterotrophic respiration and hence the flux of CO_2 released to the atmosphere is the sum of respiration from the litter and soil organic matter reservoirs. The rate of decomposition of organic matter is determined essentially by soil moisture and temperature using a Q_{10} dependence following the formulation of Krinner et al. (2005). The rate of decomposition (by respiration) depends also on the lignin fraction and the soil texture following Parton et al. (1988).

Changes in the carbon balance of the vegetation affect the energy and water balance, and hence the climate, through changes in stomatal conductance and LAI. Through its control on leaf transpiration, stomatal conductance affects latent heat flux and the surface energy balance. LAI on the other hand affects evapotranspiration because it is used to scale leaf-level to canopy level transpiration and evaporation from the interception reservoir (water intercepted by leaves).

In CNRM-ESM1, except for crops, changes in LAI don't affect the albedo of the land-surface, as it is the case in some other models. As mentioned earlier, albedo is derived from satellite observations corrected in the presence of snow, but does not depend on the changes in LAI calculated by the model. This limits the biophysical feedback from vegetation change to the atmosphere.

2.3.2 Ocean biogeochemical model

The biogeochemical model of CNRM-ESM1 is PISCES (Aumont and Bopp, 2006). This model simulates the biogeochemical cycles of oxygen, carbon and the main nutrients with 24 state variables. Macronutrients (i.e., nitrate and ammonium, phosphate, silicate)

GMDD
8, 5671–5739, 2015

and micronutrient (i.e., iron) ensure a better representation of the phytoplankton dynamics, because these 5 nutrients contribute to the nutrient limitation process (Aumont et al., 2003). PISCES represents two size-classes of phytoplankton (i.e., nanophytoplankton and diatoms). Dependence of growth to temperature is parameterized according to Eppley et al. (1969). Growth rate is also limited by the external availability in nutrients using Michaelis–Menten relationships. Diatoms differ from nanophytoplankton by their need in silicon, by higher requirements in iron (Sunda and Huntsman, 1997) and by higher half-saturation constants because of their larger mean surface-to-volume aspect ratio. Zooplankton is represented by two size-classes: microzooplankton and mesozooplankton.

PISCES can be considered as a Monod model (Monod, 1942) since it does not represent the internal concentration of nutrients into the cells. The ratios between carbon, nitrate and phosphate are kept constant to the values proposed by Takahashi et al. (1985) in all living and nonliving pools of organic matter. However, internal concentrations of iron in both phytoplankton and of silicon in diatoms are prognostically simulated. They depend on the external concentration of these nutrients, on the potential limitation by the other nutrients and on light availability.

Phytoplankton chlorophyll concentration is prognostically simulated following Geider et al. (1998) formulation. PISCES simulates semilabile dissolved organic matter, small and big sinking particles, which differ by their sinking speeds (i.e., $3\,m\,d^{-1}$ and 50 to $200\,m\,d^{-1}$, respectively). Only the internal concentrations of iron, silicon and calcite inside the sinking particles are prognostically simulated. In addition to exchange with organic carbon, dissolved inorganic carbon is also altered by the production and dissolution of calcite. Carbon chemistry in seawater is computed from the distribution of dissolved inorganic carbon and alkalinity. Calcite is prognostically simulated following Maier-Reimer (1993) and Moore et al. (2002). Alkalinity includes the contribution of carbonate, bicarbonate, borate and water ions. Oxygen is prognostically simulated using two different oxygen-to-carbon ratios, one accounting when ammonium is converted to or mineralized from organic matter, the other when oxygen is consumed during nitrifi-

GMDD
8, 5671–5739, 2015

cation. For carbon and oxygen pools, air–sea exchange follows the Wanninkhof (1992) formulation. Importantly, to ensure conservation of nitrate in the ocean, annual total nitrogen fixation should balance denitrification following Lipschultz et al. (1990), Middelburg et al. (1996) and Soetaert et al. (2000). Therefore, carbon and nitrogen cycles are decoupled to a certain degree.

The boundary conditions account for nutrient supply from three different sources: atmospheric dust deposition for iron and silicon (Jickells and Spokes, 2001; Moore et al., 2004; Tegen and Fung, 1995), rivers for carbon (Ludwig et al., 1996) and sediment mobilization for sedimentary iron (de Baar and de Jong, 2001; Johnson et al., 1999). In CNRM-ESM1, riverine input of carbon has been revised from Ludwig et al. (1996) in accounting for the interannual variability of runoff estimated with an offline SURFEX simulation over the 1948–2010 period with Princeton atmospheric forcing.

In CNRM-ESM1, the marine biophysical feedback is induced by changes in the penetration of downward irradiance in response to marine biota chlorophyll concentration. This feedback mimics the fact that light absorption in the ocean indeed depends on particle concentration and is spectrally selective (Morel, 1988). The implementation of this mechanism is fully described in Lengaigne et al. (2006) and Lengaigne et al. (2009) for an ocean forced configuration and Mignot et al. (2013) for a current ocean coupled configuration. It is derived from an accurate 61 spectral bands formulation proposed by Morel (1988) using three large wavebands: blue (400–500 nm), green (500–600 nm) and red (600–700 nm). These three bands correspond to the spectral domain of maximum absorption for chlorophyll. The chlorophyll-dependent attenuation coefficients depend on the three-dimensional chlorophyll field predicted by PISCES. They are computed at each time step from a power–law relationship fitting to the coefficients computed from the full spectral model of Morel et al. (1988). This biophysical feedback represents a major evolution from the ocean component used in Voldoire et al. (2013) and Séférian et al. (2013).

GMDD
8, 5671–5739, 2015

3 Experimental set-up

3.1 Equilibrium strategy

The CMIP5 specification requires each model to reach its equilibrium state before kicking off formal simulations, especially for long-term control experiments. To obtain the initial conditions for CNRM-ESM1 preindustrial steady state at year 1850, we first initialize the various physical and biogeochemical components of the model as described below and perform a 320 year online spin-up simulation with all 1850 external forcings (Taylor et al., 2009).

Initialization of the physical components of CNRM-ESM1 relies on previous model outputs from CNRM-CM5.1. This latter model was first initialized from World Ocean Atlas 2005 observations for salinity and temperature (Antonov et al., 2006; Locarnini et al., 2006) and spun-up for 200 years. The 801th year of the centennial long CMIP5 preindustrial run from CNRM-CM5.1 was employed as initial condition for CNRM-ESM1 preindustrial state.

Marine biogeochemical reservoirs were initialized from fields of a previous preindustrial simulation of CNRM-CM5.1 coupled to PISCES. In this previous simulation, PISCES state variables were initialized from World Ocean Atlas 1993 observations for nitrate, phosphate, silicate, and oxygen (Levitus et al., 1993) and the Global Ocean Data Analysis Project (Key et al., 2004) for alkalinity and preindustrial dissolved inorganic carbon (DIC). From this initialization, this intermediate version of the ESM was integrated online for 1100 years.

Land biogeochemical reservoirs were initialized from zero and spun-up using an online acceleration approach for soil carbon and wood during the first century of the spin-up simulation. This approach consists in updating the wood growth, the litter and soil biogeochemistry modules several times per time step with constant incoming carbon fluxes and physical conditions allowing to fill up much faster the various reservoirs of carbon. As a result of this approach, soil carbon and wood reservoirs were respectively spun-up for 21 800 and 1200 years.

GMDD
8, 5671–5739, 2015

Finally, both physical and carbon cycle components of CNRM-ESM1 benefit from an on-line adjustment under 1850 preindustrial control conditions for 400 years. Section 4.1 describes the residual drifts of the model at quasi-equilibrium state.

3.2 CMIP5 preindustrial control and historical simulations

Following CMIP5 specifications (Taylor et al., 2009), CNRM-ESM1 has performed several CMIP5 long-term core experiments and part of the tier-1 experiments.

The preindustrial control simulation, *piControl,* is integrated for 250 years using constant external forcing prescribed at 1850 conditions and starting from the last year of the on-line adjustment simulation. That is, atmospheric concentrations of greenhouse gases are set to 284.7 ppmv, 790.9, and 275.4 ppbv for CO_2, CH_4 and N_2O, respectively. Those of CFC-11, CFC-12 are set to zero. Influence of natural aerosols is prescribed using the optical depths of five types of tropospheric aerosols (black carbon, sea salt, sulfate, dust and particle organic matter) from an LMDZ-INCA simulation forced with CMIP5 prescribed emissions (Szopa et al., 2013). Stratospheric volcanic aerosols are prescribed similarly but using a long-term average climatology from a last millennium simulation performed with the NCAR model (Ammann et al., 2007).

The 20th century experiment, *historical*, is performed from year 1850 to 2005. This simulation starts from the CNRM-ESM1 states of the last year of the on-line adjustment simulation. The modern evolution of the external forcings of both atmospheric greenhouse gases and incoming solar irradiance follows the recommended yearly average observations (Taylor et al., 2009). The monthly temporal and spatial variability of the five tropospheric aerosols also rely on a LMDZ-INCA simulation (Szopa et al., 2013) while those of stratospheric sulphate aerosol concentrations from explosive volcanoes are derived from a 20th century reconstruction of the NCAR model (Ammann et al., 2003).

Note there is no land-cover change related to anthropogenic land use in the above-mentioned simulations. The fraction of vegetal cover is set to the present-day state using the in-house ECOCLIMAP database (Masson et al., 2013a). Therefore, changes

GMDD
8, 5671–5739, 2015

in physical and biogeochemical properties of the vegetation due to actual land-cover changes are excluded by design.

4 Results

4.1 Model equilibrium in the preindustrial control simulation

To illustrate the stability of CNRM-ESM1 at the end of the spin-up simulation, we show the global average values of a few variables during the 250 years of the piControl simulation (Fig. 2) and their drifts (Table 1).

In terms of energy balance, the global mean top-of-atmosphere (TOA) net radiative balance is about $3.57 \pm 0.23\,\mathrm{W\,m^{-2}}$, while the global mean net surface radiation flux (NSF) is $0.87 \pm 0.24\,\mathrm{W\,m^{-2}}$ (Fig. 2a). The imbalance in the energy budget between the surface and TOA (about $2.7\,\mathrm{W\,m^{-2}}$) is predominantly due to the non-conservation of energy of the spectral atmospheric model and, to a lesser extent, its coupling with the ocean model. Taking apart this non-conservation offset in TOA net radiation flux, there is no discernible deviation between year-to-year fluctuation between the TOA and NSF net radiation fluxes.

In terms of global-scale climate indices, the global mean surface temperature ($T_{2\,\mathrm{m}}$) and sea surface temperature (SST) over the piControl period are 12.52 ± 0.15 and $17.76 \pm 0.1\,^{\circ}\mathrm{C}$ respectively (Fig. 2b). They both display almost no drift over the duration of the piControl simulation (Table 1). We use soil wetness index (SWI) and sea surface salinity (SSS) to evaluate the stability of the simulated water cycle (Fig. 2c). These both have almost no drift (Table 1), confirming that the water cycle is closed. Also, there is no drift in both Northern Hemisphere and Southern Hemisphere sea-ice volume (NIV, SIV, respectively) for which long-term means are respectively 20.88 and $6.25 \times 10^3\,\mathrm{km^3}$ (Fig. 2d).

Regarding the simulated global carbon cycle, Fig. 2e shows that the natural carbon cycle is stable over the piControl simulation with terrestrial and oceanic carbon fluxes

GMDD
8, 5671–5739, 2015

of 0.75 ± 0.57 and $-0.94 \pm 0.13\,\mathrm{Pg\,C\,y^{-1}}$, respectively. Both terrestrial and oceanic components of the simulated carbon cycle exhibit drifts smaller than $10^{-3}\,\mathrm{Pg\,C\,y^{-1}}$ demonstrating that soil and deep ocean carbon stocks have reached a steady state. Deviation from zero in the terrestrial carbon flux is essentially explained by missing processes in ISBA such as the weathering and riverine-induced carbon transport from land to oceans (Battin et al., 2009; Regnier et al., 2013). Natural ocean carbon outgasing falls within the upper range of ocean inverse estimates (Jacobson et al., 2007; Mikaloff Fletcher et al., 2007).

4.2 Late 20th century climatology

4.2.1 Land physical drivers

In the following, we focus on the physical drivers of the global carbon cycle. From a land perspective, surface temperature ($T_{2\,\mathrm{m}}$), precipitation (PR) and photosynthetically active radiation (PAR) are the prominent factors controlling the rate of photosynthetic activity as well as the rate of autotrophic and heterotrophic respiration, and hence the net land–air exchange of carbon.

Compared to the CRUTV4 dataset (Harris et al., 2013) over the period 1986–2005, CNRM-ESM1 displays a global annual averaged bias of $-3\,^{\circ}\mathrm{C}$ in $T_{2\,\mathrm{m}}$ over continents. In Northern Hemisphere winter (DJFM, Fig. 3a) simulated $T_{2\,\mathrm{m}}$ is generally lower than the observations except for some regions (e.g., north east Siberia, south of Australia and part of Argentina). The mean bias over continents in boreal winter is about $-4\,^{\circ}\mathrm{C}$ and can reach up to $-6\,^{\circ}\mathrm{C}$ over mountain regions. Figure 3b shows that simulated summer (i.e., JJAS) $T_{2\,\mathrm{m}}$ is also generally colder than the observations ($-0.8\,^{\circ}\mathrm{C}$ in global average) over a large fraction of the continents. Only the most Northern domains of the Northern Hemisphere display a warm bias that can reach up to $3\,^{\circ}\mathrm{C}$ in the north of Canada. The geographical structure of the $T_{2\,\mathrm{m}}$ bias compares well with those detailed in (Voldoire et al., 2013). Such an agreement in the bias structure for $T_{2\,\mathrm{m}}$ was expected since both models rely on the same physical parameterizations for

GMDD
8, 5671–5739, 2015

both the atmosphere and land surface physics. Small deviations between CNRM-CM5 and CNRM-ESM1 mean state can be essentially attributed to the land carbon cycle, which appears to amplify the global average cold bias of 0.8 °C (with biases of −0.7 and −1 °C in boreal winter and summer, respectively). This cooling is due to the enhanced evapotranspiration by the interactive terrestrial biosphere compared to the fixed one in CNRM-CM5.

Figure 4 shows the regional structure of the precipitation (PR) bias of CNRM-ESM1 with respect to the GPCP observations (Adler et al., 2003). Over continents, CNRM-ESM1 slightly underestimates the amount of the seasonal PR except over Asia, the Western coast of America and Australia. The major regional bias in seasonal PR is found over Amazonia, where PR is underestimated by 2 and 5 mm day^{-1} in boreal summer and winter, respectively. Similar to state-of-the-art Earth system models, CNRM-ESM1 displays an excess of precipitation over the oceans. This excess is especially strong in the Southern part of the tropical oceans and is associated with the overestimated seasonal latitudinal migration of the ITCZ. The land biosphere biophysical coupling induces small but noticeable changes in the global hydrological cycle between CNRM-CM5 and CNRM-ESM1. The mismatch between simulated and GPCP observed PR over continents is slightly improved during the boreal winter with a bias reduced by 0.014 mm day^{-1} in CNRM-ESM1. Summer PR is similar between the two models with non-significant changes in simulated values ($< 10^{-5}$ mm day^{-1}) but their geographical patterns have been slightly degraded in CNRM-ESM1 compared to CNRM-CM5. Although weak, changes induced by the ISBA biophysical coupling slightly improve the representation of the seasonal cycle in PR over Northern mid-latitude continents by amplifying the seasonal maximum and shifting it from June in CNRM-CM5 to July in CNRM-ESM1 (Supplement).

Compared to SRB satellite-derived observations (Pinker and Laszlo, 1992), CNRM-ESM1 overestimates the photosynthetically active radiation (PAR) globally (Fig. 5). Major biases are found over continents except for some regions in the Tropics. The magnitude of the seasonal biases is weaker in Northern Hemisphere winter than in sum-

GMDD
8, 5671–5739, 2015

mer when regional biases reach up to 20–30 $W m^{-2}$ over the Western border of the continents. Regions where PAR is underestimated match reasonably well with those showing too intense precipitations compared to the GPCP dataset (Fig. 4). The general overestimation in PAR is due to the substantial underestimation in low cloud cover in CNRM-ESM1 consistent with CNRM-CM5. Biases in PAR are also found over ocean upwelling system and are linked with an underestimated fraction of stratocumulus.

4.2.2 Ocean physical drivers

From an oceanic perspective, temperature is as important as over land surface because it sets the marine biota's growth rate, playing a large role in the biological-mediated processes (e.g., export, soft tissue pump). In addition, both temperature (T) and salinity (S) control the solubility of CO_2 into seawater and the chemical-mediated air–sea exchanges of carbon. The mixed-layer depth (MLD) and the sea-ice cover (SIC) are also critical drivers of the ocean carbon cycle as they both contribute to the nutrient-to-light limitation in the high latitude oceans (Sarmiento and Gruber, 2006). In the following, we assess the representation of these drivers.

Compared to WOA2013 data products (Levitus et al., 2013), CNRM-ESM1 realistically simulates both the mean annual sea surface temperature and sea surface salinity, both in terms of amplitude and spatial distribution, as shown in Fig. 6a and b. Moderate positive biases in sea surface temperature and sea surface salinity are found in the Southern Ocean and in the Eastern boundary upwelling systems. Strong biases in sea surface salinity are found in the Labrador and Arctic Seas. While most of these biases are related to an overestimated atmospheric surface heating, biases in the Labrador Sea and in the Arctic are essentially due to erroneous representation of the mixed-layer depth and the Arctic sea-ice cover. These points will be further detailed below.

At depth, the vertical structures in T and S present moderate deviations from WOA2013 observations. T is underestimated by $\sim 2\,^{\circ}C$ within the first 1000 m of the Atlantic and Pacific oceans, except in the deep water formation zone (North Atlantic,

GMDD
8, 5671–5739, 2015

North Pacific and Southern Ocean), where the model displays positive biases. Contrasting to T, the vertical structure of S matches well with WOA2013 observations. Deviations from the observed S profile are found in deep water formation zones where haline biases tend to compensate for the warm bias in T, enabling deep convection of water masses. Thanks to this compensating mechanism, the flow of North Atlantic deep waters (NADW) fueling the Atlantic meridional overturning circulation is about 26.1 ± 2 Sv at 26.5° N in CNRM-ESM1 averaged over the 1850–2005 period. This value is stronger than the observations-derived estimate of 18 ± 5 Sv (Talley et al., 2003) or the observations from RAPID-MOCHA monitoring array over 2004–2007 estimating the flow at about 18.5 ± 4.9 Sv (Johns et al., 2011). In the Southern Ocean, the flow of Antarctic bottom water (AABW) is about 11.6 ± 1 Sv in CNRM-ESM1 averaged over the 1850–2005 period. This flow of AABW is in agreement with the deep flow of waters compared to the observed estimate of 10 ± 2 Sv (Orsi et al., 1999). Consequently, the flow of deep water masses in CNRM-ESM1 is stronger than that of CNRM-CM5 (Séférian et al., 2013; Voldoire et al., 2013). As detailed in several intercomparison studies (de Lavergne et al., 2014; Heuzé et al., 2013; Sallée et al., 2013; Séférian et al., 2013), CNRM-CM5 substantially underestimated the flow of AABW leading to an erroneous distribution of hydrodynamical and biogeochemical fields at depth. Here, although stronger than the observation-based estimates, the flow of NADW and AABW improves the deep ocean ventilation as well as the distribution of tracers at depth (Sect. 4.2.5).

As mentioned above, an accurate representation of spatial and temporal MLD is essential for numerous ocean biogeochemical processes. For example, winter mixing entrains carbon- and nutrient-rich deep waters to the surface, which play an important role in the transfer of CO_2 across the sea-to-air interface. In summer, MLD contributes to the nutrient-to-light limitation of the phytoplankton growth in high-latitude oceans. MLD_{max} and MLD_{min} are respectively used as a proxy of the winter and summer MLD since mixing occurs randomly during seasons in response to numerous environmental factors (wind, stratification, local instability etc. . . .) that present a large spatiotemporal

GMDD
8, 5671–5739, 2015

variability. Figure 7 presents composites of MLD_{max} and MLD_{min} over the 1986–2005 period as simulated by CNRM-ESM1 and as derived from observations (Sallée et al., 2010). Figure 7ab shows that CNRM-ESM1 reproduces well the regional pattern of MLD_{max} compared to the observation-derived estimates. However, the model tends to simulate too large and too deep mixing sites in the North Atlantic, the North Pacific and the Southern Ocean. In the North Atlantic, the larger than observed mixed volume of surface dense waters (combination of surface area and depth of the mixing zone) is at the origin of the strong flow of NADW simulated in CNRM-ESM1. In the Southern Ocean, although open ocean polynyas were observed from space in the past decades (Cavalieri et al., 1996; Comiso, 1999), their locations are erroneous in CNRM-ESM1 similarly to several other CMIP5 Earth system models (de Lavergne et al., 2014). CNRM-ESM1 simulates open ocean polynyas in the Indian basin and close to the Ross Sea but not in the Atlantic basin as observed from space between 1974 and 1976. Interestingly, CNRM-CM5 did not present such erroneous location of the open ocean polynyas as documented in Voldoire et al. (2013) and further investigated in de Lavergne et al. (2014). The use of GELATO6 in CNRM-ESM1 compared to GELATO5 in CNRM-CM5 in addition to the change in coupling frequency might be at the origin of this model-data disagreement.

Compared to the observation-derived estimates, the MLD_{min} is reasonably well simulated in CNRM-ESM1. Compared to the previous model versions (Séférian et al., 2013; Voldoire et al., 2013), CNRM-ESM1 fails at reproducing the deepest values of mixing in the Southern Ocean and the Tropics. These are tightly linked to the current parameterization of the ocean mixing employed in CNRM-ESM1 implying a contribution of the surface wind energy to the mixing below the MLD.

Similarly to the MLD, SIC is an important driver of the ocean carbon cycle. It constitutes a physical barrier for exchange of CO_2 between the ocean and the atmosphere leading to an accumulation of carbon-rich waters below the sea ice (Takahashi, 2009). It also plays a large role in the seasonal timing of algal blooms (Wassmann et al., 2010). Compared to the MLD, seasonal variations of sea ice are strongly and directly respon-

GMDD
8, 5671–5739, 2015

sive to the seasonal fluctuations of atmospheric forcing. Therefore, it matters that the model is able to accurately capture the spatial distribution and timing of annual minimal and maximal sea ice covers in both Hemispheres. For this purpose, we evaluate differences between composites of simulated and observed SIC (Cavalieri et al., 1996) for September and March over the 1986–2005 period (Fig. 8). In the Arctic Ocean, CNRM-ESM1 underestimates SIC in the Beaufort, Chukchi and East Siberian seas in September, while too much sea ice tends to be present in the Barents Sea (Fig. 8a). In March, SIC is largely overestimated in the Barents and nordic seas, as well as in the Bering and Okhotsk seas on the Pacific Ocean side, showing that the simulated winter sea ice edge spreads too far south and east in these regions (represented with iso-15 % in Fig. 8c). On the contrary, SIC is slightly underestimated in the Labrador Sea and Baffin Bay in March (Fig. 8c). This too far North ice edge comes along with positive SST biases in this region (Fig. 6a), and explains why the simulated deep convection zone is too large and shifted northward in CNRM-ESM1 as shown in Fig. 7.

In the Antarctic Ocean, Fig. 8b shows that the spatial structures of SIC biases mirror somehow the model-data mismatch in MLD as shown in Fig. 7b. That is, in austral winter, CNRM-ESM1 underestimates SIC where erroneous open ocean deep convection zones are located, namely offshore Wilkes Land in the Indian Ocean sector (Fig. 8b). Conversely, too much sea ice is simulated in the Atlantic Ocean sector. As in CNRM-CM5.1, simulated summer Antarctic SIC is strongly underestimated, with very little sea ice surviving summer melt in the Weddell and Ross Seas (Fig. 8d).

4.2.3 Comparison with previous model version

In the following, we compare the skill of CNRM-ESM1 to the closest version of CNRM-CM5 climate model, called CNRM-CM5-2. Figure 9 summarizes skill-assessment metrics for CNRM-ESM1 and CNRM-CM5-2 in terms of major physical drivers of the global carbon cycle.

The Taylor diagram for land surface physical drivers clearly demonstrates that CNRM-ESM1 and CNRM-CM5 display comparable skills except for PR (Fig. 9a). Most

GMDD
8, 5671–5739, 2015

of the differences in skills are indeed not significant at a 95 % confidence level; models differ solely in terms of PR for which CNRM-ESM1 produces slightly weaker correlation coefficients.

Over the ocean, Fig. 9b shows further differences between both models. The weakest difference in skill concerns SST for which both models display good agreement with WOA2013. Regarding the MLD, CNRM-ESM1 displays a slightly better agreement than CNRM-CM5-2 with observation-derived MLD (Sallée et al., 2010) in terms of correlation but strongly overestimates the spatial variations of this field. Major differences are noticeable for SSS. CNRM-ESM1's skill is clearly lower than that of CNRM-CM5-2. To investigate this difference, we have computed skill of PR over the ocean since this latter contributes to the spatiotemporal distribution of the SSS concomitantly to the runoff and the sea-ice seasonal cycle. Skill in PR over the ocean is similar for both models (blue diamonds on Fig. 9b). A similar finding is noticed for simulated runoff (not shown). Therefore the difference in simulated SSS between the two models can be attributed to the revised water conservation interface and erroneous distribution of sea-ice cover (Supplement). Besides, changes in coupling frequency (i.e. 24 to 6 h) might be at the origin of differences in skills between the two models.

From the small differences in skill between the two models, we can assume that the inclusion of the global carbon cycle and the biophysical coupling have not noticeably altered the simulated mean-state climate in CNRM-ESM1 compared to that of CNRM-CM5-2.

4.2.4 Terrestrial carbon cycle

Now that the physical drivers of the global carbon cycle have been evaluated, we assess the ability of CNRM-ESM1 to replicate available modern observations of the terrestrial carbon cycle. We focus on gross primary productivity (GPP), vegetation autotrophic respiration (Ra) and soil organic carbon content (cSoil) that control the net natural fluxes of CO_2 on land. Simulated budget of vegetation biomass and total ecosystem respiration (TER, sum of autotrophic and heterotrophic respirations) are

GMDD
8, 5671–5739, 2015

evaluated against available published estimates. While we can assess the capability of CNRM-ESM1 to fix and emit carbon on land, it is important to note that the CO_2 fluxes due to land-use changes are not taken into account in this analysis.

To evaluate CNRM-ESM1 GPP, we rely on two streams of data, namely the FluxNet-MTE (Jung et al., 2011) and the MOD17 satellite-derived observations (Running et al., 2004). Figure 10 shows that the amplitude of annual mean GPP as simulated by CNRM-ESM1 is slightly too strong compared to the observed estimates. The largest model-data mismatch is found in the Tropics between 10° N and 20° S, where CNRM-ESM1 simulates erroneous patterns of high GPP (values). Over Amazonia, CNRM-ESM1 fails to reproduce the zonal gradient of GPP. Regions of high GPP are in association with overestimated PAR and, to a lesser extend, underestimated PR in summer (Figs. 4 and 5, respectively; Supplement). The geographical structure of simulated GPP fits the observed over the African and Asian rain forest but its amplitude is overestimated by about $3\,\mathrm{g\,C\,m^{-2}\,day^{-1}}$. This regional overestimation impacts both the zonal and global GPP budget, which are larger than the published estimates except > 60° N (Table 2). This stronger-than-observed GPP constitutes a systematic bias of the current version of ISBA. In an offline simulation, (Carrer et al., 2013b) show that ISBA forced with Princeton university forcings (REF) overestimates global GPP by $60\,\mathrm{Pg\,C\,y^{-1}}$. Regional biases in GPP are partly compensated by overestimated Ra (Fig. 11). Simulated Ra agrees reasonably well with satellite-derived estimates except in the Tropics. This bias compensation between GPP and Ra is analyzed in detail by Joetzjer et al. (2015). In this study, the authors demonstrate that the current parameterizations of Ra and water stress in ISBA are not adequate for tropical broadleaf trees. Considering that these results were deduced from offline simulations forced with in situ observations, we can assume here that biases in GPP and Ra result from a combination of erroneous ecophysiological parameterizations and biases in physical drivers in CNRM-ESM1.

Despite these biases, the global partitioning between vegetation biomass and soil carbon is realistic with 596.7 and 2105 Pg C compared to the observed estimates of 560 ± 94 (DeFries et al., 1999) and 1750 ± 250 Pg C (Houghton, 2007), respectively.

GMDD
8, 5671–5739, 2015

Furthermore, the geographical structure of cSoil agrees well with Harmonized World Soil Database (FAO, 2012) except in the Northern Hemisphere (Fig. 12). Although several processes are missing in ISBA to accurately simulate high-latitude carbon stock (e.g., permafrost dynamics, bacterial degradation of the litter, fire-induced turnover etc. . . .), a part of cSoil underestimation can be attributed to the summer warm bias in near-surface temperature (Fig. 3b). This latter tends to enhance heterotrophic respiration of the soil, reducing the soil organic matter ($R > 0.6$, Supplement).

Table 2 shows that CNRM-ESM1 overestimates globally terrestrial ecosystem respiration (TER) when compared to the up-scaled measurements of FluxNet-MTE. In the Tropics, simulated TER fluxes are 32 % higher compared to the FluxNet-MTE estimates. As mentioned above, this bias is essentially due to an unrealistic Ra, which amounts to 72 % of TER over the sector in the model. Table 2 shows that the simulated TER is 126.9 $\mathrm{Pg\,C\,y^{-1}}$, larger than estimates published by Jung et al. (2011) of $96.4 \pm 6.0\,\mathrm{Pg\,C\,y^{-1}}$. Nevertheless, the simulated net land carbon sink (LCS), which can be estimated by subtracting TER from GPP, is 2.19 $\mathrm{Pg\,C\,y^{-1}}$ and remains within the range of values estimated from various observation-based methods (IPCC, 2007, 2013; Le Quéré et al., 2014).

4.2.5 Ocean carbon cycle

Compared to the terrestrial carbon cycle, the ocean carbon cycle has already been implemented in previous versions of CNRM-CM5 (Séférian et al., 2013). The modeled marine biogeochemistry components have already benefited from detailed evaluation against modern observations (Frölicher et al., 2014; Séférian et al., 2013), analyses of future projections (Laufkötter et al., 2015) and sensitivity benchmarking (Schwinger et al., 2014). The major difference between CNRM-ESM1 and previous versions of CNRM-CM5 including a marine biogeochemistry module lies in the representation of ocean tracers in the deep ocean. Figure 13 shows that the representation of oxygen, phosphate, nitrate and silicate fields was improved in CNRM-ESM1 at depth, except around 1000 m where the strong flow of NADW tends to alter the distribution of tracers.

GMDD
8, 5671–5739, 2015

Below 1500 m, the tracer distribution is in reasonable agreement with the observations with correlation coefficients ~ 0.8. This represents a noticeable improvement with respect to the CNRM-CM5 oxygen distribution ($R \sim 0.4$). In addition to nutrients, the vertical distribution of carbon-related fields like dissolved inorganic carbon has been substantially improved in CNRM-ESM1 compared to CNRM-CM5 (Supplement), showing a much better agreement with GLODAP observations (Key et al., 2004; Sabine et al., 2004).

In term of carbon cycling into the ocean, Fig. 14 shows the simulated mean annual sea–air CO_2 fluxes over 1986–2005 together with observation-based estimates by Takahashi et al. (2010) using 2000 as a single reference year. While the model broadly agrees with the observations in terms of spatial variation for regions of carbon sink (i.e., North Atlantic, North Pacific and between 50–40° S), it displays a too strong source of carbon to the atmosphere in the equatorial Pacific and in the Southern Ocean. In the equatorial Pacific, the model-data mismatch is likely related to the decision of Takahashi et al. (2010) to exclude observations from El Niño years from their analysis. Since surface ocean pCO_2 of the Eastern tropical Pacific during El Niño events tends to be lower than the long-term mean, the Lamont–Doherty Earth Observatory (LDEO) climatology tends to underestimate outgasing of CO_2 in the equatorial Pacific over the 1986–2005 period. This hypothesis is validated when comparing model results against recent data products derived from statistical Monte-Carlo Markov Chain or Neural Network gapfilling methods (Landschützer et al., 2014; Majkut et al., 2014). In the Southern Ocean, the model-data mismatch is especially pronounced south of 60° S. This bias in $fgCO_2$ is associated with overestimated mixing (Fig. 7), which tends to bring too much deep carbon-rich water masses to the surface, enhancing the outgasing of CO_2. CNRM-ESM1 results display similar discrepancy when compared to other recent observation-derived data products which agree in a moderate CO_2 outgasing south of 60° S (not shown). That said, simulated patterns of sea-to-air carbon fluxes in this domain qualitatively agree with the data in showing a combination of source and sink regions.

GMDD
8, 5671–5739, 2015

The storage of anthropogenic CO_2 by the oceans (CO_2^{ANTH}, Fig. 15) provides a complementary view of the ocean carbon fluxes by revealing the chronology of the ocean CO_2 uptake from preindustrial to modern state. Here, we have chosen to stick to the available observation-derived estimates, GLODAP, which use year 1994 as a single reference year (Key et al., 2004; Sabine et al., 2004). In order to account for the interannual variability of the simulated fields, we chose to analyze yearly average results from CNRM-ESM1 over 1990–2005 (Fig. 15). Besides, computation of CO_2^{ANTH} is not straightforward since natural and anthropogenic pools of carbon are not treated separately in PISCES. We approximate consequently CO_2^{ANTH} from the difference between modern and preindustrial stocks of dissolved inorganic carbon. Negative values were set to zero in the computation since they are essentially generated from differences in simulated interannual variability. Ideally, this computation would have required a historical simulation with constant preindustrial atmospheric CO_2 for the sea-to-air CO_2 fluxes. Figure 15 shows that the maximum CO_2^{ANTH} is concentrated in the North Atlantic region. This feature is linked to the large-scale circulation in the surface layer of the ocean, which converges in the North Atlantic, before being exported to depth with the flow of NADW (Pérez et al., 2013). The Southern Ocean also stores a large fraction of CO_2^{ANTH} in association with the subduction of modal and intermediate water masses (Sallée et al., 2012). Compared to this global view, CNRM-ESM1 displays features that are broadly consistent with the CO_2^{ANTH} estimates. However, the stronger flow of NADW and AABW leads to a depletion of the stock of CO_2^{ANTH} between 0 and 1200 m (Fig. 14c). This mechanism leads to an increase in the stock of CO_2^{ANTH} at depth. Over the 1850–1994 period, the model takes up a total of 100.8 Pg C, which is in agreement with the observations that suggest a net uptake of 106 ± 17 Pg C over the same period (Khatiwala et al., 2013; Sabine et al., 2004).

GMDD
8, 5671–5739, 2015

4.2.6 Ecosystem dynamics

In this section, we assess the performance of CNRM-ESM1 in terms of two ecosystem dynamics parameters, namely the peak leaf area index (LAI_{max}) and the ocean surface chlorophyll (Chl). Both parameters are monitored continuously from space since the 1980s and the 1990s, respectively, providing a suitable set of indirect observations to assess the simplified ecosystem representation embedded in Earth system models.

Regarding LAI_{max}, Fig. 16 shows that the model agrees well with satellite-derived observations (Zhu et al., 2013) except over Africa and Asia with overestimated values. As such, this ecosystem parameter behaves similarly to GPP and Ra, responding to biases in PR and PAR. In the Northern mid-latitudes, LAI_{max} is slightly overestimated compared to the satellite-derived observations but remains in the low range of values simulated by other CMIP5 Earth system models evaluated in Anav et al. (2013b). Using an offline simulation forced with atmospheric reanalyzes (Szczypta et al., 2014) shows similar biases in LAI over Northern Europe as those noticed in CNRM-ESM1. It is thus likely that missing processes like forest and crop management or fire-induced disturbance might induce an overestimated LAI_{max}.

Regarding ocean Chl, Fig. 17 shows that CNRM-ESM1 displays a reasonable agreement with satellite-derived observations (O'Reilly et al., 1998). Although regional patterns of Chl concentrations were improved compared to that of CNRM-CM5 (Séférian et al., 2013), major model discrepancies are found in oligotrophic gyres and equatorial upwellings. Biases are more pronounced in the Southern Hemisphere where the model fails to produce very low Chl in the Southern Pacific gyres. CNRM-ESM1 also fails at capturing Western border high Chl concentrations in relation with the equatorial upwelling. Underestimated Chl concentrations in upwelling systems are essentially due to biases in surface wind forcing but also to the coarse horizontal and vertical resolution of the ocean model. This model limitation partly explains why Chl concentrations are underestimated in high-latitude oceans. In these domains, high coastal concentra-

GMDD
8, 5671–5739, 2015

tions are captured from satellite sensors but cannot be resolved by the model due to its coarse resolution.

4.3 Recent evolution of the climate system

In the present section, we analyze the transient response of various climate indices to the recent climate change from 1901 to 2005. We focus on the near-surface temperature ($T_{2\,m}$), the September Arctic sea-ice extent (SIE), the 0–2000 m ocean heat content (OHC) as well as the land and ocean carbon sinks (LCS, OCS, respectively). Over this period, these climate indices are analyzed with their nominal values except for $T_{2\,m}$ and OHC that are represented with respect to the 1961–1990 and the 1955–2005 periods, respectively. Figure 18 illustrates how these various climate indices evolve from 1901 to 2005 and Table 3 summarizes their mean-state, interannual variability (IAV) and decadal trends over the 1986–2005 period.

Figure 18 shows that the transient response of $T_{2\,m}$ agrees reasonably well with modern observations (Morice et al., 2012). At the end of the last decades of the historical simulation (i.e. 1986–2005), CNRM-ESM1 overestimates the $T_{2\,m}$ increase, a discrepancy widely shared by other CMIP5 Earth system models (Huber and Knutti, 2014; Kosaka and Xie, 2013; Meehl et al., 2011; Watanabe et al., 2013). The amplitude of the simulated recent IAV is in line with the observations (Table 3). In particular, the model simulates strong cooling followed by stronger warming following the 1991 mount Pinatubo eruption. Contrasting with temperature, the simulated SIE poorly agrees with observation-based estimates (Cavalieri et al., 1996; Comiso, 1999; Rayner et al., 2003). Indeed, CNRM-ESM1 underestimates the mean-state SIE by about 2×10^6 km^2 and overestimates not only the IAV but also the decadal decrease in extent (Table 3). Therefore, in terms of Arctic sea ice, the skill of CNRM-ESM1 is similar to CNRM-CM5 as detailed in Massonnet et al. (2012). A better agreement is found for OHC for which CNRM-ESM1 results agree with observation-based estimates in term of mean-state and decadal trends (Fig. 18, Table 3). Only the recent IAV in OHC is underestimated by the model, but this latter is poorly constrained by the observations in regards of the

GMDD
8, 5671–5739, 2015

little amount of data available below 1000 m (Levitus et al., 2012, 2009; Willis et al., 2004).

The recent evolution of LCS and OCS agrees with the range of observation-based and model-derived estimates (Le Quéré et al., 2015; Takahashi et al., 2010) with an uptake of CO_2 of about 2.1 and 1.7 $Pg\,C\,y^{-1}$ for land and ocean, respectively (Table 3). Underestimation in mean-state OCS is essentially due to the stronger river-induced offshore outgasing of CO_2 which is about 0.9 $Pg\,C\,y^{-1}$ in the model and assumed to be of 0.45 $Pg\,C\,y^{-1}$ in the observation-derived estimates. Both OCS and LCS IAV are underestimated in CNRM-ESM1 compared to the estimates. For OCS IAV, this behavior is found in most ocean biogeochemical models as shown in Wanninkhof et al. (2013). Indeed, simulated IAV from biogeochemical models substantially contrasts with the large IAV estimated from atmospheric inversion which also contributes to the mix of observations and model reconstructions that compose the data (Le Quéré et al., 2015). For the land carbon cycle, underestimated LCS IAV may be related to the under-sensitivity of ISBA to climate variability in contrast with the over-sensitivity to the rising CO_2, a behavior shared with other land surface process-based models (Piao et al., 2013). Note that differences in phase between simulated and estimated LCS were expected since the land sink of carbon is approximated from the difference between atmospheric growth rate, land-use emissions and ocean carbon sink (Friedlingstein et al., 2010).

5 Summary and conclusions

In this manuscript, we evaluate the ability of the Centre National de Recherches Météorologiques Earth system model version 1 (CNRM-ESM1) to reproduce the modern carbon cycle and its prominent physical drivers. CNRM-ESM1 derives from the atmosphere–ocean general circulation model CNRM-CM5 (Voldoire et al., 2013) that has contributed to CMIP5 and to the fifth IPCC assessment report. This model employs the same resolution and components as CNRM-CM5 although it uses updated versions of the atmospheric model (ARPEGE-CLIMAT v6.1), surface scheme (SURFEXv7.3)

GMDD
8, 5671–5739, 2015

and sea-ice model (GELATO6) in addition to a 6 h coupling frequency. Several biophysical coupling processes are enabled in CNRM-ESM1 thanks to the terrestrial carbon cycle module ISBA (Gibelin et al., 2008) and the marine biogeochemistry module PISCES (Aumont and Bopp, 2006). They consist of the land biosphere-mediated evapotranspiration feedback and the ocean biota heat-trapping feedbacks.

Since an earlier version of CNRM-CM5 including the marine biogeochemistry module PISCES was distributed and used in several studies (Frölicher et al., 2014; Laufkötter et al., 2015; Schwinger et al., 2014; Séférian et al., 2013), the inclusion of the terrestrial carbon cycle module ISBA constitutes the major advancement in the CNRM-ESM1 development. Although the ISBA terrestrial carbon cycle module was developed at CNRM in the 2000s, it had never been coupled to an atmosphere–ocean model and run for long climate simulations. Here, we show that ISBA embedded in CNRM-ESM1 reproduces the general pattern of the vegetation and soil carbon stock over the last decades. Although the photosynthesis scheme in ISBA differs from the other state-of-the-art process-based models (e.g., Dalmonech et al., 2014), the model displays similar behavior. That is, it overestimates both the land-vegetation gross primary productivity and the terrestrial ecosystem respiration. The compensation between these two fluxes leads to a correct land carbon sink over the modern period that agrees with the most up-to-date estimates (Friedlingstein et al., 2010; Jung et al., 2011; Le Quéré et al., 2015). The largest model-data mismatch is found in the Tropics where the gross uptake of CO_2 from the vegetation is strongly compensated by an overestimated autotrophic respiration. Maybe apart from this compensating mechanism, our analysis demonstrates that the terrestrial carbon cycle module of CNRM-ESM1 displays discrepancies similar to other IPCC-Class vegetation models (Supplement, see also details in Anav et al. (2013a) and Piao et al., 2013). The future effort in development will be oriented towards a better parameterization of the carbon absorption and respiration by the vegetation in association with a better representation of ecophysiological processes as detailed in Joetzjer et al. (2015). Further processes like fire-induced dis-

GMDD
8, 5671–5739, 2015

turbance, mortality or linked with permafrost will also be included in order to improve the representation of the live biomass and soil carbon pool.

Regarding the marine biogeochemistry component, the global distribution of biogeochemical tracers such as oxygen, nutrients and carbon-related fields has been improved with respect to an earlier model version (Séférian et al., 2013). This change is attributed to improved water conservation in the ocean–sea ice model as well as a higher coupling frequency that induces a stronger northward flow of deep water masses from the Southern Ocean. While the simulated anthropogenic carbon storage agrees with 1994 observation-based estimates, the ocean carbon sink falls within the lower range of the combination of observation and model estimates over the recent years (Le Quéré et al., 2015). This slightly underestimated carbon sink is attributed to larger outgasing of natural CO_2 induced by the riverine input, which fits the upper range of values documented in the fifth IPCC assessment report (IPCC, 2013). Future development will target a better representation of this flux of carbon in close relationship with the recent development on the land surface hydrology (Decharme et al., 2013).

We show that CNRM-ESM1 displays results comparable to those of CNRM-CM5 in spite of the inclusion of the global carbon cycle and various biophysical feedbacks. Simulated near-surface temperature, precipitation, incoming shortwave radiation over continents as well as temperature, salinity and mixed-layer depth over oceans broadly agree with observations or satellite-derived product. Except for the salinity and the mixed-layer depth, CNRM-ESM1 display quite similar skill at simulating physical drivers of the global carbon cycle compared to CNRM-CM5. Such a comparison demonstrates the reliability of this model to produce suitable simulations for future climate change projection and impacts studies.

In addition to preindustrial control and historical simulations discussed in this manuscript, several other simulations were performed with CNRM-ESM1 following both the CMIP5 and GeoMIP experimental design. The CNRM-ESM1 model outputs (referred as “CNRM-ESM1”) are available for download on ESGF under CMIP5 and GeoMIP projects.

GMDD
8, 5671–5739, 2015

Code availability

A number of model codes developed at CNRM, or in collaboration with CNRM scientists, is available as Open Source code (see https://opensource.cnrm-game-meteo.fr/ and http://www.nemo-ocean.eu/). However, this is not the case for the Earth system model presented in this paper. Part of its code is nevertheless available upon request from the authors of the paper.

The Supplement related to this article is available online at doi:10.5194/gmdd-8-5671-2015-supplement.

Acknowledgements. This work was supported by Météo-France, CNRS and CERFACS. We particularly acknowledge the support of the team in charge of the CNRM-CM climate model. Supercomputing time was provided by the Météo-France/DSI supercomputing center. Data are published thanks to the ESGF and IS-ENES2 projects. Finally, we are grateful to C. Frauen for her kind advices on the nuances of the English language.

References

Adler, R. F., Huffman, G. J., Chang, A., Ferraro, R., Xie, P.-P., Janowiak, J., Rudolf, B., Schneider, U., Curtis, S., Bolvin, D., Gruber, A., Susskind, J., Arkin, P., and Nelkin, E.: The version-2 Global Precipitation Climatology Project (GPCP) monthly precipitation analysis (1979–present), J. Hydrometeorol., 4, 1147–1167, doi:10.1175/1525-7541(2003)004<1147:TVGPCP>2.0.CO;2, 2003.

Ammann, C. M., Meehl, G. A., Washington, W. M., and Zender, C. S.: A monthly and latitudinally varying volcanic forcing dataset in simulations of 20th century climate, Geophys. Res. Lett., 30, 1657, doi:10.1029/2003GL016875, 2003.

Ammann, C. M., Joos, F., Schimel, D. S., Otto-Bliesner, B. L., and Tomas, R. A.: Solar influence on climate during the past millennium: results from transient simulations

GMDD
8, 5671–5739, 2015

with the NCAR Climate System Model, P. Natl. Acad. Sci. USA, 104, 3713–3718, doi:10.1073/pnas.0605064103, 2007.
Anav, A., Friedlingstein, P., Kidston, M., Bopp, L., Ciais, P., Cox, P., Jones, C., Jung, M., Myneni, R., and Zhu, Z.: Evaluating the land and ocean components of the global carbon cycle in the CMIP5 earth system models, J. Climate, 26, 6801–6843, doi:10.1175/JCLI-D-12-00417.1, 2013a.
Anav, A., Murray-Tortarolo, G., Friedlingstein, P., Sitch, S., Piao, S., and Zhu, Z.: Evaluation of land surface models in reproducing satellite derived Leaf Area Index over the high-latitude Northern Hemisphere. Part II: Earth system models, Remote Sensing, 5, 3637–3661, doi:10.3390/rs5083637, 2013b.
Antonov, J. I., Locarnini, R., Boyer, T., Mishonov, A., Garcia, H., and Levitus, S.: World Ocean Atlas 2005 Volume 2: Salinity, in: NOAA Atlas NESDIS 62, edited by: Levitus, S., 182 pp., US Gov. Print. Off., Washington, D. C., USA, 2006.
Arora, V. K., Boer, G. J., Friedlingstein, P., Eby, M., Jones, C. D., Christian, J. R., Bonan, G., Bopp, L., Brovkin, V., Cadule, P., Hajima, T., Ilyina, T., Lindsay, K., Tjiputra, J. F., and Wu, T.: Carbon–concentration and carbon–climate feedbacks in CMIP5 earth system models, J. Climate, 26, 5289–5314, doi:10.1175/JCLI-D-12-00494.1, 2013.
Aumont, O. and Bopp, L.: Globalizing results from ocean in situ iron fertilization studies, Global Biogeochem. Cy., 20, GB2017, doi:10.1029/2005GB002591, 2006.
Aumont, O., Maier-Reimer, E., Blain, S., and Monfray, P.: An ecosystem model of the global ocean including Fe, Si, P colimitations, Global Biogeochem. Cy., 17, 1060, doi:10.1029/2001GB001745, 2003.
Axell, L.: Wind-driven internal waves and Langmuir circulations in a numerical ocean model of the southern Baltic Sea, J. Geophys. Res.-Oceans, 107, 25-1–25-20, doi:10.1029/2001JC000922, 2002.
Barnier, B., Madec, G., Penduff, T., Molines, J.-M., Treguier, A.-M., Sommer, J., Beckmann, A., Biastoch, A., Böning, C., Dengg, J., Derval, C., Durand, E., Gulev, S., Remy, E., Talandier, C., Theetten, S., Maltrud, M., McClean, J., and Cuevas, B.: Impact of partial steps and momentum advection schemes in a global ocean circulation model at eddy-permitting resolution, Ocean Dynam., 56, 543–567, doi:10.1007/s10236-006-0082-1, 2006.
Battin, T. J., Luyssaert, S., Kaplan, L. A., Aufdenkampe, A. K., Richter, A., and Tranvik, L. J.: The boundless carbon cycle, Nat. Geosci., 2, 598–600, doi:10.1038/ngeo618, 2009.

GMDD
8, 5671–5739, 2015

Blanke, B. and Delecluse, P.: Variability of the tropical Atlantic Ocean simulated by a general circulation model with two different mixed-layer physics, J. Phys. Oceanogr., 23, 1363–1388, doi:10.1175/1520-0485(1993)023<1363:VOTTAO>2.0.CO;2, 1993.
Boone, A., Calvet, J.-C., and Noilhan, J.: Inclusion of a third soil layer in a land surface scheme using the force–restore method, J. Appl. Meteorol., 38, 1611–1630, doi:10.1175/1520-0450(1999)038<1611:IOATSL>2.0.CO;2, 1999.
Bouillon, S., Morales Maqueda, M. Á., Legat, V., and Fichefet, T.: An elastic–viscous–plastic sea ice model formulated on Arakawa B and C grids, Ocean Model., 27, 174–184, 2009.
Bretherton, F. P.: Earth system science and remote sensing, Proc. IEEE, 73, 1118–1127, doi:10.1109/PROC.1985.13242, 1985.
Calvet, J.-C.: Investigating soil and atmospheric plant water stress using physiological and micrometeorological data, Agr. Forest Meteorol., 103, 229–247, 2000.
Calvet, J.-C. and Soussana, J.-F.: Modelling CO_2-enrichment effects using an interactive vegetation SVAT scheme, Agr. Forest Meteorol., 108, 129–152, doi:10.1016/S0168-1923(01)00235-0, 2001.
Calvet, J.-C., Noilhan, J., Roujean, J.-L., Bessemoulin, P., Cabelguenne, M., Olioso, A., and Wigneron, J.-P.: An interactive vegetation SVAT model tested against data from six contrasting sites, Agr. Forest Meteorol., 92, 73–95, doi:10.1016/S0168-1923(98)00091-4, 1998.
Calvet, J.-C., Rivalland, V., Picon-Cochard, C., and Guehl, J.-M.: Modelling forest transpiration and CO_2 fluxes – response to soil moisture stress, Agr. Forest Meteorol., 124, 143–156, 2004.
Calvet, J.-C., Gibelin, A.-L., Roujean, J.-L., Martin, E., Le Moigne, P., Douville, H., and Noilhan, J.: Past and future scenarios of the effect of carbon dioxide on plant growth and transpiration for three vegetation types of southwestern France, Atmos. Chem. Phys., 8, 397–406, doi:10.5194/acp-8-397-2008, 2008.
Cariolle, D. and Brard, D.: The distribution of ozone and active stratospheric species: results of a two-dimensional atmospheric model, in: Atmospheric Ozone, edited by: Zerefos, C. S. and Ghazi, A., Springer Netherlands, 77–81, 1985.
Cariolle, D. and Teyssèdre, H.: A revised linear ozone photochemistry parameterization for use in transport and general circulation models: multi-annual simulations, Atmos. Chem. Phys., 7, 2183–2196, doi:10.5194/acp-7-2183-2007, 2007.
Carrer, D., Ceamanos, X., and Roujean, J. L.: Analysis of snow-free vegetation and bare soil albedos and application to numerical weather prediction, Presented at the Geoscience and

GMDD
8, 5671–5739, 2015

Remote Sensing Symposium (IGARSS), Melbourne, VIC, 21–26 July 2013, IEEE International IS, 3789–3792, 2013a.
Carrer, D., Roujean, J. L., Lafont, S., Calvet, J.-C., Boone, A., Decharme, B., Delire, C., and Gastellu-Etchegorry, J. P.: A canopy radiative transfer scheme with explicit FAPAR for the interactive vegetation model ISBA-A-gs: impact on carbon fluxes, J. Geophys. Res.-Biogeosci., 118, 888–903, doi:10.1002/jgrg.20070, 2013b.
Cavalieri, D. J., Parkinson, C. L., Gloersen, P., and Zwally, H.: Sea Ice Concentrations from Nimbus-7 SMMR and DMSP SSM/I-SSMIS Passive Microwave Data, years 1978–2014, NASA DAAC at the National Snow and Ice Data Center, Boulder, Colorado, USA, 1996.
Collatz, G. J., Ribas-Carbo, M., and Berry, J. A.: Coupled photosynthesis-stomatal conductance model for leaves of C_4 plants, Funct Plant Biol., 19, 519–538, 1992.
Comiso, J. C.: Bootstrap Sea Ice Concentrations from Nimbus-7 SMMR and DMSP SSM/I-SSMIS (Version 2), 2nd edn., National Snow and Ice Data Center, Boulder, Colorado, USA, 1999.
Cox, P., Betts, R., Jones, C., Spall, S., and Totterdell, I.: Acceleration of global warming due to carbon-cycle feedbacks in a coupled climate model, Nature, 408, 184–187, 2000.
Dalmonech, D., Foley, A. M., Anav, A., Friedlingstein, P., Friend, A. D., Kidston, M., Willeit, M., and Zaehle, S.: Challenges and opportunities to reduce uncertainty in projections of future atmospheric CO_2: a combined marine and terrestrial biosphere perspective, Biogeosciences Discuss., 11, 2083–2153, doi:10.5194/bgd-11-2083-2014, 2014.
de Baar, H. J. W. and de Jong, J. T. M.: Distributions, sources and sinks of iron in seawater, in: The Biogeochemistry of Iron in Seawater, edited by: Turner, D. R. and Hunter, K. A., John Wiley, Hoboken, NJ, USA, 85–121, 2001.
Decharme, B., Martin, E., and Faroux, S.: Reconciling soil thermal and hydrological lower boundary conditions in land surface models, J. Geophys. Res.-Atmos., 118, 7819–7834, doi:10.1002/jgrd.50631, 2013.
DeFries, R. S., Field, C. B., Fung, I., Collatz, G. J., and Bounoua, L.: Combining satellite data and biogeochemical models to estimate global effects of human-induced land cover change on carbon emissions and primary productivity, Global Biogeochem. Cy., 13, 803–815, doi:10.1029/1999GB900037, 1999.
de Lavergne, C., Palter, J. B., Galbraith, E. D., Bernardello, R., and Marinov, I.: Cessation of deep convection in the open Southern Ocean under anthropogenic climate change, Nature Clim. Change, 4, 278–282, doi:10.1038/nclimate2132, 2014.

GMDD
8, 5671–5739, 2015

Douville, H., Royer, J. F., and Mahfouf, J. F.: A new snow parameterization for the Météo-France climate model, Clim. Dynam., 12, 21–35–35, doi:10.1007/BF00208760, 1995.
Eppley, R. W., Rogers, J. N., and McCarthy, J. J.: Half-saturation constants for uptake of nitrate and ammonium by marine phytoplankton, Limnol. Oceanogr., 14, 912–920, 1969.
Eyring, V., Arblaster, J. M., and Cionni, I.: Long-term ozone changes and associated climate impacts in CMIP5 simulations, J. Geophys. Res. Atmos., 118, 5029–5060, doi:10.1002/jgrd.50316, 2013.
Fairall, C. W., Bradley, E. F., Hare, J. E., Grachev, A. A., and Edson, J. B.: Bulk parameterization of air–sea fluxes: updates and verification for the COARE algorithm, J. Climate, 16, 571–591, doi:10.1175/1520-0442(2003)016<0571:BPOASF>2.0.CO;2, 2003.
FAO/IIASA/ISRIC/ISSCAS/JRC: Harmonized World Soil Database (version 1.10), FAO, Rome, Italy and IIASA, Laxenburg, Austria, 2012.
Farquhar, G. D., Caemmerer, S., and Berry, J. A.: A biochemical model of photosynthetic CO_2 assimilation in leaves of C_3 species, Planta, 149, 78–90, doi:10.1007/BF00386231, 1980.
Fetterer, F., Knowles, K., Meier, W., and Savoie, M.: Sea Ice Index, 2014 edn., National Snow and Ice Data Center, Boulder, Colorado, USA, doi:10.7265/N5QJ7F7W, 2002.
Friedlingstein, P. and Prentice, I. C.: Carbon-climate feedbacks: a review of model and observation based estimates, Curr. Opin. Env. Sust., 2, 251–257, doi:10.1016/j.cosust.2010.06.002, 2010.
Friedlingstein, P., Houghton, R. A., Marland, G., Hackler, J., Boden, T. A., Conway, T. J., Canadell, J. G., Raupach, M. R., Ciais, P., and Le Quéré, C.: Update of CO_2 emissions, Nat. Geosci., 3, 811–812, doi:10.1038/ngeo1022, 2010.
Friedlingstein, P., Meinshausen, M., Arora, V. K., Jones, C. D., Anav, A., Liddicoat, S. K., and Knutti, R.: Uncertainties in CMIP5 climate projections due to carbon cycle feedbacks, J. Climate, 27, 511–526, doi:10.1175/JCLI-D-12-00579.1, 2013.
Frölicher, T. L., Sarmiento, J. L., Paynter, D. J., Dunne, J. P., Krasting, J. P., and Winton, M.: Dominance of the Southern Ocean in anthropogenic carbon and heat uptake in CMIP5 models, J. Climate, 28, 862–886, doi:10.1175/JCLI-D-14-00117.1, 2014.
Geider, R., MacIntyre, H., and Kana, T.: A dynamic regulatory model of phytoplanktonic acclimation to light, nutrients, and temperature, Limnol. Oceanogr., 43, 679–694, 1998.
Gibelin, A.-L., Calvet, J.-C., Roujean, J.-L., Jarlan, L., and Los, S. O.: Ability of the land surface model ISBA-A-gs to simulate leaf area index at the global scale: comparison with satellites products, J. Geophys. Res., 111, D18102, doi:10.1029/2005JD006691, 2006.

GMDD
8, 5671–5739, 2015

Gibelin, A.-L., Calvet, J.-C., and Viovy, N.: Modelling energy and CO_2 fluxes with an interactive vegetation land surface model-Evaluation at high and middle latitudes, Agr. Forest Meteorol., 148, 1611–1628, doi:10.1016/j.agrformet.2008.05.013, 2008.

Goudriaan, J., van Laar, H. H., van Keulen, H., and Louwerse, W.: Photosynthesis, CO_2 and plant production, in: NATO ASI Science, vol. 86, edited by: Day, W. and Atkin, R. K., Springer US, Boston, MA, USA, 107–122, 1985.

Hajima, T., Kawamiya, M., Watanabe, M., Kato, E., Tachiiri, K., Sugiyama, M., Watanabe, S., Okajima, H., and Ito, A.: Modeling in Earth system science up to and beyond IPCC AR5, Progress in Earth and Planetary Science, 1, 29–25, doi:10.1186/s40645-014-0029-y, 2014.

Harris, I., Jones, P. D., Osborn, T. J., and Lister, D. H.: Updated high-resolution grids of monthly climatic observations – the CRU TS3.10 Dataset, Int. J. Climatol., 34, 623–642, doi:10.1002/joc.3711, 2013.

Heuzé, C., Heywood, K. J., Stevens, D. P., and Ridley, J. K.: Southern Ocean bottom water characteristics in CMIP5 models, Geophys. Res. Lett., 40, 1409–1414, doi:10.1002/grl.50287, 2013.

Houghton, R. A.: Balancing the global carbon budget, Annu. Rev. Earth Pl. Sc., 35, 313–347, doi:10.1146/annurev.earth.35.031306.140057, 2007.

Huber, M. and Knutti, R.: Natural variability, radiative forcing and climate response in the recent hiatus reconciled, Nat. Geosci., 7, 651–656, doi:10.1038/ngeo2228, 2014.

Hunke, E. C. and Dukowicz, J. K.: An elastic–viscous–plastic model for sea ice dynamics, J. Phys. Oceanogr., 27, 1849–1867, doi:10.1175/1520-0485(1997)027<1849:AEVPMF>2.0.CO;2, 1997.

IPCC: Climate Change 2007: The Physical Science Basis, edited by: Solomon, S., Qin, D., Manning, M., Chen, Z., Marquis, M., Averyt, K. B., Tignor, M., and Miller, H. L., Cambridge University Press, Cambridge, UK, and New York, NY, USA, 2007.

IPCC: Climate Change 2013: The Physical Science Basis, edited by: Stoker,T. F., Qin, D., Plattner, G., Tignor, M., Allen, S. K., Boschung, J., Nauels, A., Xia, Y., Bex, V., and Midgley, P. M., Cambridge Univ. Press, Cambridge, UK, and New York, NY, USA, 2013.

Jacobs, C. M. J., van den Hurk, B. M. M., and de Bruin, H. A. R.: Stomatal behaviour and photosynthetic rate of unstressed grapevines in semi-arid conditions, Agr. Forest Meteorol., 80, 111–134, 1996.

GMDD
8, 5671–5739, 2015

Jacobson, A. R., Mikaloff Fletcher, S. E., Gruber, N., Sarmiento, J. L., and Gloor, M.: A joint atmosphere–ocean inversion for surface fluxes of carbon dioxide: 1. Methods and global-scale fluxes, Global Biogeochem. Cy., 21, GB1019, doi:10.1029/2005GB002556, 2007.

Jickells, T. and Spokes, L.: Atmospheric iron inputs to the oceans, in: The Biogeochemistry of Iron in Seawater, edited by: Turner, D. R. and Hunter, K. A., John Wiley, Hoboken, NJ, USA, 85–121, 2001.

Joetzjer, E., Delire, C., Douville, H., Ciais, P., Decharme, B., Fisher, R., Christoffersen, B., Calvet, J. C., da Costa, A. C. L., Ferreira, L. V., and Meir, P.: Predicting the response of the Amazon rainforest to persistent drought conditions under current and future climates: a major challenge for global land surface models, Geosci. Model Dev., 7, 2933–2950, doi:10.5194/gmd-7-2933-2014, 2014.

Joetzjer, E., Delire, C., Douville, H., Ciais, P., Decharme, B., Carrer, D., Verbeeck, H., De Weirdt, M., and Bonal, D.: Improving the ISBA$_{CC}$ land surface model simulation of water and carbon fluxes and stocks over the Amazon forest, Geosci. Model Dev., 8, 1709–1727, doi:10.5194/gmd-8-1709-2015, 2015.

Johns, W. E., Baringer, M. O., Beal, L. M., Cunningham, S. A., Kanzow, T., Bryden, H. L., Hirschi, J. J. M., Marotzke, J., Meinen, C. S., Shaw, B., and Curry, R.: Continuous, array-based estimates of Atlantic Ocean heat transport at 26.5° N, J. Climate, 24, 2429–2449, doi:10.1175/2010JCLI3997.1, 2011.

Johnson, K., Chavez, F., and Friederich, G.: Continental-shelf sediment as a primary source of iron for coastal phytoplankton, Nature, 398, 697–700, 1999.

Jung, M., Reichstein, M., Margolis, H. A., Cescatti, A., Richardson, A. D., Arain, M. A., Arneth, A., Bernhofer, C., Bonal, D., Chen, J., Gianelle, D., Gobron, N., Kiely, G., Kutsch, W., Lasslop, G., Law, B. E., Lindroth, A., Merbold, L., Montagnani, L., Moors, E. J., Papale, D., Sottocornola, M., Vaccari, F., and Williams, C.: Global patterns of land–atmosphere fluxes of carbon dioxide, latent heat, and sensible heat derived from eddy covariance, satellite, and meteorological observations, J. Geophys. Res., 116, G00J07, doi:10.1029/2010JG001566, 2011.

Key, R., Kozyr, A., Sabine, C., Lee, K., Wanninkhof, R., Bullister, J., Feely, R., Millero, F., Mordy, C., and Peng, T.: A global ocean carbon climatology: results from Global Data Analysis Project (GLODAP), Global Biogeochem. Cy., 18, GB4031, doi:10.1029/2004GB002247, 2004.

GMDD
8, 5671–5739, 2015

Khatiwala, S., Tanhua, T., Mikaloff Fletcher, S., Gerber, M., Doney, S. C., Graven, H. D., Gruber, N., McKinley, G. A., Murata, A., Ríos, A. F., and Sabine, C. L.: Global ocean storage of anthropogenic carbon, Biogeosciences, 10, 2169–2191, doi:10.5194/bg-10-2169-2013, 2013.

Koch-Larrouy, A., Madec, G., Bouruet-Aubertot, P., Gerkema, T., Bessières, L., and Molcard, R.: On the transformation of Pacific water into Indonesian throughflow water by internal tidal mixing, Geophys. Res. Lett., 34, L04604, doi:10.1029/2006GL028405, 2007.

Koch-Larrouy, A., Lengaigne, M., Terray, P., Madec, G., and Masson, S.: Tidal mixing in the Indonesian Seas and its effect on the tropical climate system, Clim. Dynam., 34, 891–904, doi:10.1007/s00382-009-0642-4, 2010.

Kosaka, Y. and Xie, S.-P.: Recent global-warming hiatus tied to equatorial Pacific surface cooling, Nature, 501, 403–407, doi:10.1038/nature12534, 2013.

Krinner, G., Viovy, N., de Noblet-Ducoudré, N., Ogée, J., Polcher, J., Friedlingstein, P., Ciais, P., Sitch, S., and Prentice, I. C.: A dynamic global vegetation model for studies of the coupled atmosphere–biosphere system, Global Biogeochem. Cy., 19, 1–33, 2005.

Landschützer, P., Gruber, N., Bakker, D. C. E., and Schuster, U.: Recent variability of the global ocean carbon sink, Global Biogeochem. Cy., 28, 927–949, doi:10.1002/2014GB004853, 2014.

Laufkötter, C., Vogt, M., Gruber, N., Aita-Noguchi, M., Aumont, O., Bopp, L., Buitenhuis, E., Doney, S. C., Dunne, J., Hashioka, T., Hauck, J., Hirata, T., John, J., Le Quéré, C., Lima, I. D., Nakano, H., Seferian, R., Totterdell, I., Vichi, M., and Völker, C.: Drivers and uncertainties of future global marine primary production in marine ecosystem models, Biogeosciences Discuss., 12, 3731–3824, doi:10.5194/bgd-12-3731-2015, 2015.

Lengaigne, M., Menkes, C., Aumont, O., Gorgues, T., Bopp, L., André, J.-M., and Madec, G.: Influence of the oceanic biology on the tropical Pacific climate in a coupled general circulation model, Clim. Dynam., 28, 503–516, doi:10.1007/s00382-006-0200-2, 2006.

Lengaigne, M., Madec, G., Bopp, L., Menkes, C., Aumont, O., and Cadule, P.: Bio-physical feedbacks in the Arctic Ocean using an Earth system model, Geophys. Res. Lett., 36, L21602, doi:10.1029/2009GL040145, 2009.

Le Quéré, C., Moriarty, R., Andrew, R. M., Peters, G. P., Ciais, P., Friedlingstein, P., Jones, S. D., Sitch, S., Tans, P., Arneth, A., Boden, T. A., Bopp, L., Bozec, Y., Canadell, J. G., Chini, L. P., Chevallier, F., Cosca, C. E., Harris, I., Hoppema, M., Houghton, R. A., House, J. I., Jain, A. K., Johannessen, T., Kato, E., Keeling, R. F., Kitidis, V., Klein Goldewijk, K., Koven, C.,

GMDD
8, 5671–5739, 2015

Landa, C. S., Landschützer, P., Lenton, A., Lima, I. D., Marland, G., Mathis, J. T., Metzl, N., Nojiri, Y., Olsen, A., Ono, T., Peng, S., Peters, W., Pfeil, B., Poulter, B., Raupach, M. R., Regnier, P., Rödenbeck, C., Saito, S., Salisbury, J. E., Schuster, U., Schwinger, J., Séférian, R., Segschneider, J., Steinhoff, T., Stocker, B. D., Sutton, A. J., Takahashi, T., Tilbrook, B., van der Werf, G. R., Viovy, N., Wang, Y.-P., Wanninkhof, R., Wiltshire, A., and Zeng, N.: Global carbon budget 2014, Earth Syst. Sci. Data, 7, 47–85, doi:10.5194/essd-7-47-2015, 2015.

Levitus, S., Conkright, M. E., Reid, J. L., Najjar, R. G., and Mantyla, A.: Distribution of nitrate, phosphate and silicate in the world oceans, Prog. Oceanogr., 31, 245–273, 1993.

Levitus, S., Antonov, J. I., Boyer, T. P., Locarnini, R. A., Garcia, H. E., and Mishonov, A. V.: Global ocean heat content 1955–2008 in light of recently revealed instrumentation problems, Geophys. Res. Lett., 36, L07608, doi:10.1029/2008GL037155, 2009.

Levitus, S., Antonov, J. I., Boyer, T. P., Baranova, O. K., Garcia, H. E., Locarnini, R. A., Mishonov, A. V., Reagan, J. R., Seidov, D., Yarosh, E. S., and Zweng, M. M.: World ocean heat content and thermosteric sea level change (0–2000 m), 1955–2010, Geophys. Res. Lett., 39, L10603, doi:10.1029/2012GL051106, 2012.

Levitus, S., Antonov, J. I., Baranova, O. K., Boyer, T. P., Coleman, C. L., Garcia, H. E., Grodsky, A. I., Johnson, D. R., Locarnini, R. A., Mishonov, A. V., Reagan, J. R., Sazama, C. L., Seidov, D., Smolyar, I., Yarosh, E. S., and Zweng, M. M.: The World Ocean Database TI, Data Science Journal, 12, WDS229–WDS234, 2013.

Lipschultz, F., Wofsy, S. C., Ward, B. B., Codispoti, L. A., Friedrich, G., and Elkins, J. W.: Bacterial transformations of inorganic nitrogen in the oxygen-deficient waters of the eastern tropical South Pacific Ocean, Deep-Sea Res., 37, 1513–1541, doi:10.1016/0198-0149(90)90060-9, 1990.

Locarnini, R. A., Mishonov, A. V., Antonov, J. I., Boyer, T. P., Garcia, H. E., Baranova, O. K., Zweng, M. M., and Johnson, D. R.: World Ocean Atlas 2005 Volume 1: Temperature, edited by: Levitus, S., NOAA Atlas NESDIS 61, US Government Printing Office, Washington, DC, USA, 2006.

Ludwig, W., Probst, J., and Kempe, S.: Predicting the oceanic input of organic carbon by continental erosion, Global Biogeochem. Cy., 10, 23–41, 1996.

Madec, G.: NEMO Ocean Engine, Institut Pierre-Simon Laplace (IPSL), France, available at: http://www.nemo-ocean.eu/About-NEMO/Reference-manuals (last access: November 2013), 2008.

GMDD
8, 5671–5739, 2015

Maier-Reimer, E.: Geochemical cycles in an ocean general circulation model. Preindustrial tracer distributions, Global Biogeochem. Cy., 7, 645, doi:10.1029/93GB01355, 1993.
Majkut, J. D., Sarmiento, J. L., and Rodgers, K. B.: A growing oceanic carbon uptake: results from an inversion study of surface pCO_2 data, Global Biogeochem. Cy., 28, 335–351, doi:10.1002/2013GB004585, 2014.
Masson, V., Champeaux, J.-L., Chauvin, F., Meriguet, C., and Lacaze, R.: A global database of land surface parameters at 1-km resolution in meteorological and climate models, J. Climate, 16, 1261–1282, doi:10.1175/1520-0442(2003)16<1261:AGDOLS>2.0.CO;2, 2013a.
Masson, V., Le Moigne, P., Martin, E., Faroux, S., Alias, A., Alkama, R., Belamari, S., Barbu, A., Boone, A., Bouyssel, F., Brousseau, P., Brun, E., Calvet, J.-C., Carrer, D., Decharme, B., Delire, C., Donier, S., Essaouini, K., Gibelin, A.-L., Giordani, H., Habets, F., Jidane, M., Kerdraon, G., Kourzeneva, E., Lafaysse, M., Lafont, S., Lebeaupin Brossier, C., Lemonsu, A., Mahfouf, J.-F., Marguinaud, P., Mokhtari, M., Morin, S., Pigeon, G., Salgado, R., Seity, Y., Taillefer, F., Tanguy, G., Tulet, P., Vincendon, B., Vionnet, V., and Voldoire, A.: The SURFEXv7.2 land and ocean surface platform for coupled or offline simulation of earth surface variables and fluxes, Geosci. Model Dev., 6, 929–960, doi:10.5194/gmd-6-929-2013, 2013b.
Massonnet, F., Fichefet, T., Goosse, H., Bitz, C. M., Philippon-Berthier, G., Holland, M. M., and Barriat, P.-Y.: Constraining projections of summer Arctic sea ice, The Cryosphere, 6, 1383–1394, doi:10.5194/tc-6-1383-2012, 2012.
Meehl, G. A., Arblaster, J. M., Fasullo, J. T., Hu, A., and Trenberth, K. E.: Model-based evidence of deep-ocean heat uptake during surface-temperature hiatus periods, Nature Climate Change, 1, 360–364, doi:10.1038/nclimate1229, 2011.
Mellor, G. and Blumberg, A.: Wave breaking and ocean surface layer thermal response, J. Phys. Oceanogr., 34, 693–698, doi:10.1175/2517.1, 2004.
Merryfield, W., Holloway, G., and Gargett, A.: A global ocean model with double-diffusive mixing, J. Phys. Oceanogr., 29, 1124–1142, 1999.
Middelburg, J., Soetaert, K., Herman, P., and Heip, C.: Denitrification in marine sediments: a model study, Global Biogeochem. Cy., 10, 661–673, 1996.
Mignot, J., Swingedouw, D., Deshayes, J., Marti, O., Talandier, C., Séférian, R., Lengaigne, M., and Madec, G.: On the evolution of the oceanic component of the IPSL climate models from CMIP3 to CMIP5: a mean state comparison, Ocean Model., 72, 167–184, doi:10.1016/j.ocemod.2013.09.001, 2013.

GMDD
8, 5671–5739, 2015

Mikaloff Fletcher, S. E., Gruber, N., Jacobson, A. R., Gloor, M., Doney, S. C., Dutkiewicz, S., Gerber, M., Follows, M., Joos, F., Lindsay, K., Menemenlis, D., Mouchet, A., Müller, S. A., and Sarmiento, J. L.: Inverse estimates of the oceanic sources and sinks of natural CO_2 and the implied oceanic carbon transport, Global Biogeochem. Cy., 21, GB1010, doi:10.1029/2006GB002751, 2007.

Monod, J.: Recherches sur la croissance des cultures bactériennes, Hermann, Paris, 1942.

Moore, J., Doney, S., Kleypas, J., Glover, D., and Fung, I.: An intermediate complexity marine ecosystem model for the global domain, Deep-Sea Res. Pt. II, 49, 403–462, 2002.

Moore, J., Doney, S., and Lindsay, K.: Upper ocean ecosystem dynamics and iron cycling in a global three-dimensional model, Global Biogeochem. Cy., 18, GB4028, doi:10.1029/2004GB002220, 2004.

Morel, A.: Optical modeling of the upper ocean in relation to its biogenous matter content (Case-I Waters), J. Geophys. Res.-Oceans, 93, 10749–10768, 1988.

Morice, C. P., Kennedy, J. J., Rayner, N. A., and Jones, P. D.: Quantifying uncertainties in global and regional temperature change using an ensemble of observational estimates: the HadCRUT4 data set, J. Geophys. Res., 117, D08101, doi:10.1029/2011JD017187, 2012.

Noilhan, J. and Planton, S.: A simple parameterization of land surface processes for meteorological models, Mon. Weather Rev., 117, 536–549, doi:10.1175/1520-0493(1989)117<0536:ASPOLS>2.0.CO;2, 1989.

Oki, T. and Sud, Y. C.: Design of Total Runoff Integrating Pathways (TRIP) – a global river channel network, Earth Interact., 2, 1–36, 1997.

O'Reilly, J. E., Maritorena, S., Mitchell, B. G., Siegel, D. A., Carder, K. L., Garver, S. A., Kahru, M., and McClain, C.: Ocean color chlorophyll algorithms for SeaWiFS, J. Geophys. Res., 103, 24937–24953, doi:10.1029/98JC02160, 1998.

Orsi, A., Johnson, G., and Bullister, J.: Circulation, mixing, and production of Antarctic bottom water, Prog. Oceanogr., 43, 55–109, doi:10.1016/S0079-6611(99)00004-X, 1999.

Parton, W. J., Stewart, J. W. B., and Cole, C. V.: Dynamics of C, N, P and S in grassland soils: a model, Biogeochemistry, 5, 109–131, doi:10.1007/BF02180320, 1988.

Pérez, F. F., Mercier, H., Vázquez-Rodríguez, M., Lherminier, P., Velo, A., Pardo, P. C., Rosón, G., and Ríos, A. F.: Atlantic Ocean CO_2 uptake reduced by weakening of the meridional overturning circulation, Nat. Geosci., 6, 146–152, doi:10.1038/ngeo1680, 2013.

Piao, S., Sitch, S., Ciais, P., Friedlingstein, P., Peylin, P., Wang, X., Ahlström, A., Anav, A., Canadell, J. G., Cong, N., Huntingford, C., Jung, M., Levis, S., Levy, P. E., Li, J., Lin, X.,

GMDD
8, 5671–5739, 2015

Lomas, M. R., Lu, M., Luo, Y., Ma, Y., Myneni, R. B., Poulter, B., Sun, Z., Wang, T., Viovy, N., Zaehle, S., and Zeng, N.: Evaluation of terrestrial carbon cycle models for their response to climate variability and to CO_2 trends, Glob. Change Biol., 19, 2117–2132, doi:10.1111/gcb.12187, 2013.

Pinker, R. T. and Laszlo, I.: Modeling surface solar irradiance for satellite applications on a global scale, J. Appl. Meteorol., 31, 194–211, doi:10.1175/1520-0450(1992)031<0194:MSSIFS>2.0.CO;2, 1992.

Rawlins, M. A., McGuire, A. D., Kimball, J. K., Dass, P., Lawrence, D., Burke, E., Chen, X., Delire, C., Koven, C., MacDougall, A., Peng, S., Rinke, A., Saito, K., Zhang, W., Alkama, R., J. Bohn, T., Ciais, P., Decharme, B., Gouttevin, I., Hajima, T., Ji, D., Krinner, G., Lettenmaier, D. P., Miller, P., Moore, J. C., Smith, B., and Sueyoshi, T.: Assessment of model estimates of land–atmosphere CO_2 exchange across Northern Eurasia, Biogeosciences Discuss., 12, 2257–2305, doi:10.5194/bgd-12-2257-2015, 2015.

Rayner, N. A., Parker, D. E., Horton, E. B., Folland, C. K., Alexander, L. V., Rowell, D. P., Kent, E. C., and Kaplan, A.: Global analyses of sea surface temperature, sea ice, and night marine air temperature since the late nineteenth century, J. Geophys. Res., 108, 4407, doi:10.1029/2002JD002670, 2003.

Regnier, P., Friedlingstein, P., Ciais, P., Mackenzie, F. T., Gruber, N., Janssens, I. A., Laruelle, G. G., Lauerwald, R., Luyssaert, S., Andersson, A. J., Arndt, S., Arnosti, C., Borges, A. V., Dale, A. W., Gallego-Sala, A., Godderis, Y., Goossens, N., Hartmann, J., Heinze, C., Ilyina, T., Joos, F., LaRowe, D. E., Leifeld, J., Meysman, F. J. R., Munhoven, G., Raymond, P. A., Spahni, R., Suntharalingam, P., and Thullner, M.: Anthropogenic perturbation of the carbon fluxes from land to ocean, Nat. Geosci., 6, 597–607, doi:10.1038/ngeo1830, 2013.

Running, S. W., Nemani, R. R., Heinsch, F. A., Zhao, M., Reeves, M., and Hashimoto, H.: A continuous satellite-derived measure of global terrestrial primary production, BioScience, 54, 547–560, available at: http://bioscience.oxfordjournals.org/content/54/6/547.abstract (last access: November 2014), 2004.

Sabine, C., Feely, R., Gruber, N., Key, R., Lee, K., Bullister, J., Wanninkhof, R., Wong, C., Wallace, D., Tilbrook, B., Millero, F., Peng, T., Kozyr, A., Ono, T., and Rios, A.: The oceanic sink for anthropogenic CO_2, Science, 305, 367–371, doi:10.1126/science.1097403, 2004.

Salas y Mélia, D.: A global coupled sea ice–ocean model, Ocean Model., 4, 137–172, doi:10.1016/S1463-5003(01)00015-4, 2002.

GMDD
8, 5671–5739, 2015

Sallée, J., Speer, K., and Rintoul, S. R.: Zonally asymmetric response of the Southern Ocean mixed-layer depth to the Southern Annular Mode, Nat. Geosci., 3, 273–279, doi:10.1038/ngeo812, 2010.

Sallée, J.-B., Matear, R. J., Rintoul, S. R., and Lenton, A.: Localized subduction of anthropogenic carbon dioxide in the Southern Hemisphere oceans, Nat. Geosci., 5, 579–584, doi:10.1038/ngeo1523, 2012.

Sallée, J. B., Shuckburgh, E., Bruneau, N., Meijers, A. J. S., Bracegirdle, T. J., Wang, Z., and Roy, T.: Assessment of Southern Ocean water mass circulation and characteristics in CMIP5 models: historical bias and forcing response, J. Geophys. Res.-Oceans, 118, 1830–1844, doi:10.1002/jgrc.20135, 2013.

Sander, S. P., Golden, D. M., Kurylo, M. J., and Moortgat, G. K.: BEACON eSpace at Jet Propulsion Laboratory: chemical kinetics and photochemical data for use in Atmospheric Studies, Evaluation Number 15, JPL Publication 06-2, Jet Propulsion Laboratory, Pasadena, USA, 2006.

Sarmiento, J. L. and Gruber, N.: Ocean Biogeochemical Dynamics, Princeton University Press, Princeton, New Jersey, USA, 526 pp., 2006.

Sarrat, C., Noilhan, J., Dolman, A. J., Gerbig, C., Ahmadov, R., Tolk, L. F., Meesters, A. G. C. A., Hutjes, R. W. A., Ter Maat, H. W., Pérez-Landa, G., and Donier, S.: Atmospheric CO_2 modeling at the regional scale: an intercomparison of 5 meso-scale atmospheric models, Biogeosciences, 4, 1115–1126, doi:10.5194/bg-4-1115-2007, 2007.

Schwinger, J., Tjiputra, J. F., Heinze, C., Bopp, L., Christian, J. R., Gehlen, M., Ilyina, T., Jones, C. D., Salas-Mélia, D., Segschneider, J., Séférian, R., and Totterdell, I.: Non-linearity of ocean carbon cycle feedbacks in CMIP5 earth system models, J. Climate, 27, 3869–3888, doi:10.1175/JCLI-D-13-00452.1, 2014.

Séférian, R., Bopp, L., Gehlen, M., Orr, J., Ethé, C., Cadule, P., Aumont, O., Salas y Mélia, D., Voldoire, A., and Madec, G.: Skill assessment of three earth system models with common marine biogeochemistry, Clim. Dynam., 40, 2549–2573, doi:10.1007/s00382-012-1362-8, 2013.

Séférian, R., Ribes, A., and Bopp, L.: Detecting the anthropogenic influences on recent changes in ocean carbon uptake, Geophys. Res. Lett., 41, 5968–5977, doi:10.1002/2014GL061223, 2014.

GMDD
8, 5671–5739, 2015

Simmons, H., Jayne, S., St Laurent, L., and Weaver, A.: Tidally driven mixing in a numerical model of the ocean general circulation, Ocean Model., 6, 245–263, doi:10.1016/S1463-5003(03)00011-8, 2004.

Soetaert, K., Middelburg, J., Herman, P., and Buis, K.: On the coupling of benthic and pelagic biogeochemical models, Earth-Sci. Rev., 51, 173–201, 2000.

Sunda, W. and Huntsman, S.: Interrelated influence of iron, light and cell size on marine phytoplankton growth, Nature, 390, 389–392, 1997.

Szczypta, C., Decharme, B., Carrer, D., Calvet, J.-C., Lafont, S., Somot, S., Faroux, S., and Martin, E.: Impact of precipitation and land biophysical variables on the simulated discharge of European and Mediterranean rivers, Hydrol. Earth Syst. Sci., 16, 3351–3370, doi:10.5194/hess-16-3351-2012, 2012.

Szczypta, C., Calvet, J.-C., Maignan, F., Dorigo, W., Baret, F., and Ciais, P.: Suitability of modelled and remotely sensed essential climate variables for monitoring Euro-Mediterranean droughts, Geosci. Model Dev., 7, 931–946, doi:10.5194/gmd-7-931-2014, 2014.

Szopa, S., Balkanski, Y., Schulz, M., Bekki, S., Cugnet, D., Fortems-Cheiney, A., Turquety, S., Cozic, A., Déandreis, C., Hauglustaine, D., Idelkadi, A., Lathière, J., Lefèvre, F., Marchand, M., Vuolo, R., Yan, N., and Dufresne, J.-L.: Aerosol and ozone changes as forcing for climate evolution between 1850 and 2100, Clim. Dynam., 40, 2223–2250, doi:10.1007/s00382-012-1408-y, 2013.

Takahashi, T.: Climatological mean and decadal change in surface ocean pCO_2, and net sea–air CO_2 flux over the global oceans, Deep-Sea Res. Pt. II, 56, 554–577, doi:10.1016/j.dsr2.2008.12.009, 2009.

Takahashi, T., Broecker, W., and Langer, S.: Redfield ratio based on chemical-data from isopycnal surfaces, J. Geophys. Res.-Oceans, 90, 6907–6924, 1985.

Takahashi, T., Sutherland, S. C., and Kozyr, A.: Global ocean surface water partial pressure of CO_2 database: measurements performed during 1968–2010 (Version 2010), ORNL/CDIAC-159, NDP-088(V2010). Carbon Dioxide Information Analysis Center, Oak Ridge National Laboratory, U.S. Department of Energy, Oak Ridge, Tennessee, USA, doi:10.3334/CDIAC/OTG.NDP088(V2010), 2010.

Talley, L. D., Reid, J. L., and Robbins, P. E.: Data-based meridional overturning streamfunctions for the global ocean, J. Climate, 16, 3213–3226, doi:10.1175/1520-0442(2003)016<3213:DMOSFT>2.0.CO;2, 2003.

GMDD
8, 5671–5739, 2015

Taylor, K. E., Stouffer, R. J., and Meehl, G. A.: A Summary of the CMIP5 Experiment Design, available at: http://cmip-pcmdi.llnl.gov/cmip5 (last access: January 2013), 2009.
Tegen, I. and Fung, I.: Contribution to the atmospheric mineral aerosol load from land-surface modification, J. Geophys. Res.-Atmos., 100, 18707–18726, 1995.
Thorndike, A. S., Rothrock, D. A., Maykut, G. A., and Colony, R.: The thickness distribution of sea ice, J. Geophys. Res., 80, 4501–4513, doi:10.1029/JC080i033p04501, 1975.
Valcke, S.: The OASIS3 coupler: a European climate modelling community software, Geosci. Model Dev., 6, 373–388, doi:10.5194/gmd-6-373-2013, 2013.
Voldoire, A., Sanchez-Gomez, E., Salas y Mélia, D., Decharme, B., Cassou, C., Sénési, S., Valcke, S., Beau, I., Alias, A., Chevallier, M., Déqué, M., Deshayes, J., Douville, H., Fernandez, E., Madec, G., Maisonnave, E., Moine, M. P., Planton, S., Saint-Martin, D., Szopa, S., Tyteca, S., Alkama, R., Belamari, S., Braun, A., Coquart, L., and Chauvin, F.: The CNRM-CM5.1 global climate model: description and basic evaluation, Clim. Dynam., 40, 2091–2121, doi:10.1007/s00382-011-1259-y, 2013.
Wanninkhof, R.: A relationship between wind speed and gas exchange over the ocean, J. Geophys. Res., 97, 7373–7382, 1992.
Wanninkhof, R., Park, G.-H., Takahashi, T., Sweeney, C., Feely, R., Nojiri, Y., Gruber, N., Doney, S. C., McKinley, G. A., Lenton, A., Le Quéré, C., Heinze, C., Schwinger, J., Graven, H., and Khatiwala, S.: Global ocean carbon uptake: magnitude, variability and trends, Biogeosciences, 10, 1983–2000, doi:10.5194/bg-10-1983-2013, 2013.
Wassmann, P., Duarte, C. M., Agustí, S., and Sejr, M. K.: Footprints of climate change in the Arctic marine ecosystem, Glob. Change Biol., 17, 1235–1249, doi:10.1111/j.1365-2486.2010.02311.x, 2010.
Watanabe, M., Kamae, Y., Yoshimori, M., Oka, A., Sato, M., Ishii, M., Mochizuki, T., and Kimoto, M.: Strengthening of ocean heat uptake efficiency associated with the recent climate hiatus, Geophys. Res. Lett., 40, 3175–3179, doi:10.1002/grl.50541, 2013.
Wenzel, S., Cox, P. M., Eyring, V., and Friedlingstein, P.: Emergent constraints on climate-carbon cycle feedbacks in the CMIP5 Earth system models, J. Geophys. Res.-Biogeosci., 119, 794–807, doi:10.1002/2013JG002591, 2014.
Wetzel, P., Maier-Reimer, E., Botzet, M., Jungclaus, J., Keenlyside, N., and Latif, M.: Effects of ocean biology on the penetrative radiation in a coupled climate model, J. Climate, 19, 3973–3987, doi:10.1175/JCLI3828.1, 2006.

GMDD
8, 5671–5739, 2015

Willis, J. K., Roemmich, D., and Cornuelle, B.: Interannual variability in upper ocean heat content, temperature, and thermosteric expansion on global scales, J. Geophys. Res., 109, C12036, doi:10.1029/2003JC002260, 2004.

Zhu, Z., Bi, J., Pan, Y., Ganguly, S., Anav, A., Xu, L., Samanta, A., Piao, S., Nemani, R., and Myneni, R.: Global data sets of vegetation Leaf Area Index (LAI)3g and Fraction of Photosynthetically Active Radiation (FPAR)3g derived from Global Inventory Modeling and Mapping Studies (GIMMS) Normalized Difference Vegetation Index (NDVI3g) for the period 1981 to 2011, Remote Sensing, 5, 927–948, doi:10.3390/rs5020927, 2013.

GMDD
8, 5671–5739, 2015

Table 1. Drift in climate indices used to evaluate the equilibrium of CNRM-ESM1's physical and biogeochemical components. The drifts are computed over the 250-year long preindustrial simulation of CNRM-ESM1 for the top of the atmosphere net radiative balance (TOA), the net surface heat flux (NSF), the near-surface temperature ($T_{2\,m}$), the sea surface temperature (SST), the sea surface salinity (SSS), the soil wetness index (SWI), the northern and southern sea-ice volume (NIV and SIV, respectively) as well as the land and ocean global carbon fluxes (LCF and OCF).

	TOA [$W\,m^{-2}$]	NSF [$W\,m^{-2}$]	$T_{2\,m}$ [°C]	SST [°C]	SWI [–]	SSS [psu]	NIV [$10^3\,km^3$]	SIV [$10^3\,km^3$]	LCF [$Pg\,C\,y^{-1}$]	OCF [$Pg\,C\,y^{-1}$]
Drift [units century^{-1}]	4.4×10^{-4}	4.5×10^{-4}	-1.2×10^{-5}	9.6×10^{-5}	-1.6×10^{-5}	-1.9×10^{-5}	-4.4×10^{-3}	7.2×10^{-3}	-1.5×10^{-4}	-2.0×10^{-4}

GMDD
8, 5671–5739, 2015

Table 2. Regional and global budget of gross primary production (GPP) and terrestrial ecosystem respiration (TER) as simulated by the CNRM-ESM1 and estimated from the FluxNet-MTE data product. V in bracketsvalues indicate the ratio between the autotrophic respiration (Ra) and TER. The uncertainties for the FluxNet-MTE data product derives from the regional partitioning of global mean uncertainties published in (Jung et al., 2011). GPP and TER fluxes are determined from a yearly average over 1986–2005.

Regions	CNRM-ESM1 GPP [Pg C y^{-1}]	MTE-FluxNet	CNRM-ESM1 TER [Pg C y^{-1}]	MTE-FluxNet
High latitude north (> 60° N)	2.6	4.8 ± 0.8	2.5 (38 %)	3.1 ± 0.8
Mid-latitude north (20–60° N)	37.9	34.8 ± 2.7	36.23 (52 %)	29.9 ± 2.7
Tropics (20° S–20° N)	73.2	62.3 ± 1.9	72.58 (72 %)	54.8 ± 1.9
Mid-latitude south (20–60° S)	16.1	9.3 ± 0.6	15.6 (56 %)	8.5 ± 0.6
Global	130.0	111.3 ± 6.0	126.9 (64 %)	96.4 ± 6.0

GMDD
8, 5671–5739, 2015

Table 3. Modern mean-state, interannual variability (IAV) and decadal trends of various global climate indices: the near-surface temperature ($T_{2\,m}$), Arctic September sea-ice extent (SIE), 0–2000 m ocean heat content (OHC) as well as the land and ocean carbon sinks (LCS and OCS respectively). For LCS and OCS, positive values indicate an uptake of CO_2 by land and ocean. All metrics are computed over the 1986–2005 period for both model and observations. Decadal trends are estimated from linear regression over the 1986–2005 period. IAV is estimated from the standard deviation of the detrended time series.

		CNRM-ESM1	Observations
$T_{2\,m}$ [°C]	mean	0.43	0.30 ± 0.08 (Morice et al., 2012)
	IAV	0.13	0.10
	trend	4.0×10^{-2}	2.6×10^{-2}
SIE [10^6 km^2]	mean	4.68	6.70 ± 0.26 (Comiso, 1999; Fetterer et al., 2002; Rayner et al., 2003)
	IAV	1.14	0.46
	decadal	-16×10^{-2}	-6.8×10^{-2}
OHC [10^{22} J]	mean	3.34	3.50 ± 1.42 (Levitus et al., 2012)
	IAV	0.69	1.43
	trend	0.44	0.50
LCS [PgC y^{-1}]	mean	2.19	2.06 ± 1.0 [models] (Le Quéré et al., 2015) 2.19 ± 0.8 [Residual land carbon sink] (Friedlingstein et al., 2010)
	IAV	0.59	1.01
	trend	0.3×10^{-2}	1.8×10^{-2}
OCS [PgC y^{-1}]	mean	1.65	1.87 ± 0.4 [models] (Le Quéré et al., 2015) 2.15 ± 0.5 [obs.-models combination] 2.0 ± 0.7 (Takahashi et al., 2010)
	IAV	0.09	0.14
	trend	4.5×10^{-2}	1.8×10^{-2}

GMDD
8, 5671–5739, 2015

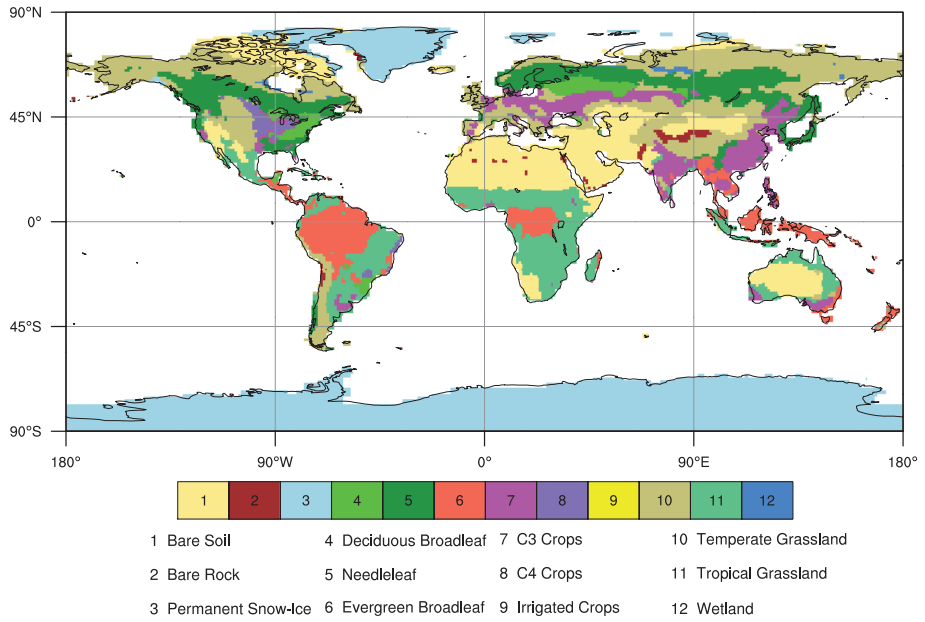

Figure 1. Fraction of dominant vegetation type as precribed in SURFEX. This fraction results from aggregation of the various ECOCLIMAP's vegetation types at 1 km resolution over the T127 CNRM-ESM1 horizontal grid (~ 1.4° nominal horizontal resolution).

GMDD
8, 5671–5739, 2015

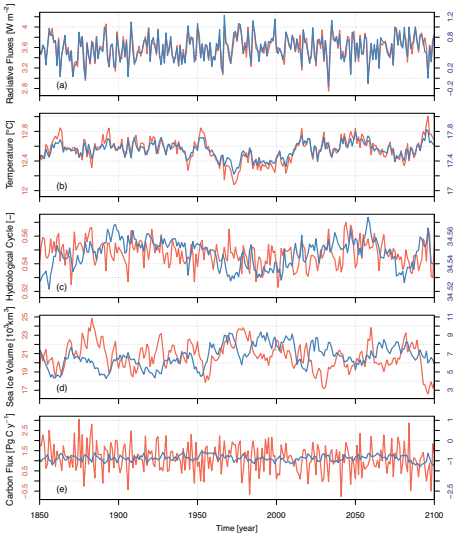

Figure 2. Time series of various climate indices along the 250-year long control simulation. **(a)** Net radiative fluxes at the top of the atmosphere (in red, left *y* axis) and surface (in blue, right *y* axis) are used to assess the stability of the climate energy flow in the model; **(b)** near-surface global average temperature (in red, left *y* axis) and global averaged sea surface temperature (in blue, right *y* axis); **(c)** soil wetness index (in red, left *y* axis) and sea surface salinity (in blue, right *y* axis) are used as proxy of the hydrological cycle; **(d)** sea ice volume in the Northern Hemisphere (in red, left *y* axis) and in the Southern Hemisphere (in blue, right *y* axis) are used to evaluate the stability of the cryosphere component in CNRM-ESM1; **(e)** global carbon fluxes over land (in red, left *y* axis) and over ocean (in blue, right *y* axis) are used to assess the equilibration of the global carbon stock. For carbon fluxes, positive (negative) fluxes indicate an uptake (outgasing) of CO_2 by land or ocean.

GMDD
8, 5671–5739, 2015

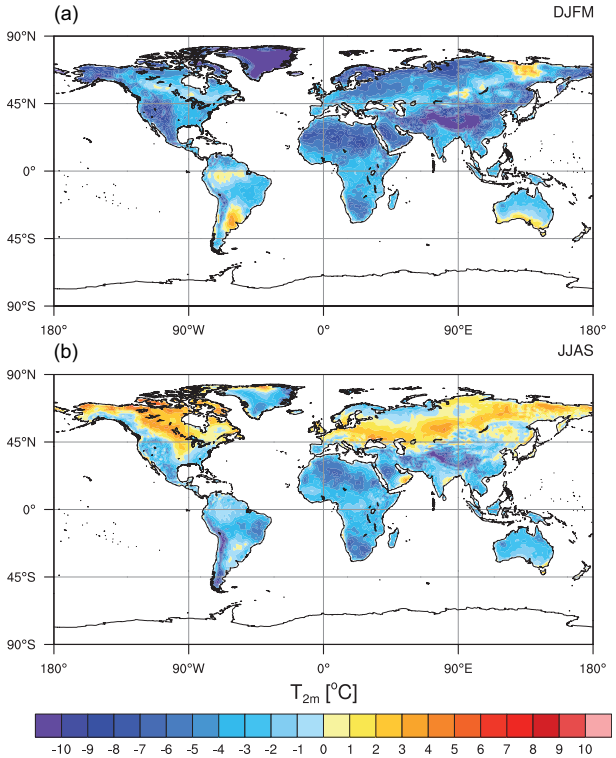

Figure 3. Biases in simulated near-surface temperature ($T_{2\,m}$) compared to the CRUTV4 observations (Harris et al., 2013) averaged 1986–2005. Winter **(a)** and summer **(b)** periods are computed from DJFM and JJAS months.

GMDD
8, 5671–5739, 2015

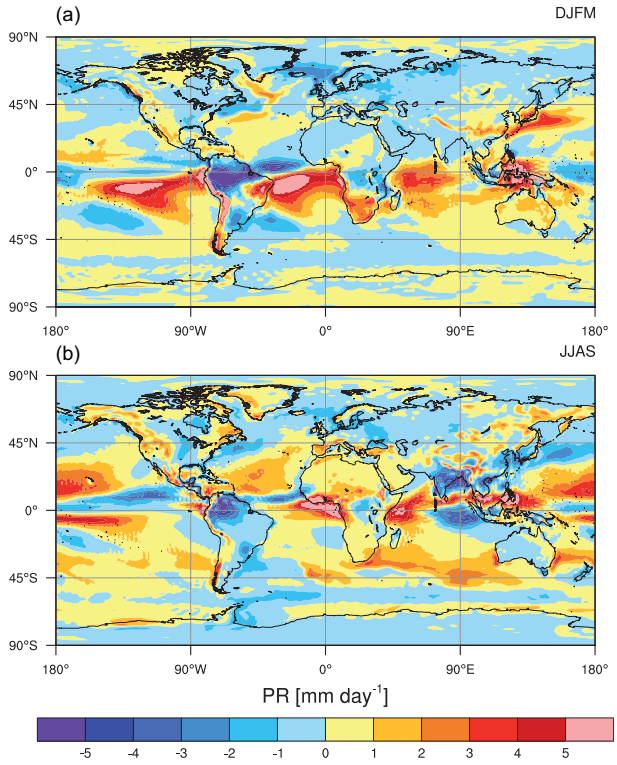

Figure 4. Biases in simulated precipitation (PR) compared to the GPCP observations (Adler et al., 2003) averaged over 1986–2005. Winter **(a)** and summer **(b)** periods are computed from DJFM and JJAS months.

GMDD
8, 5671–5739, 2015

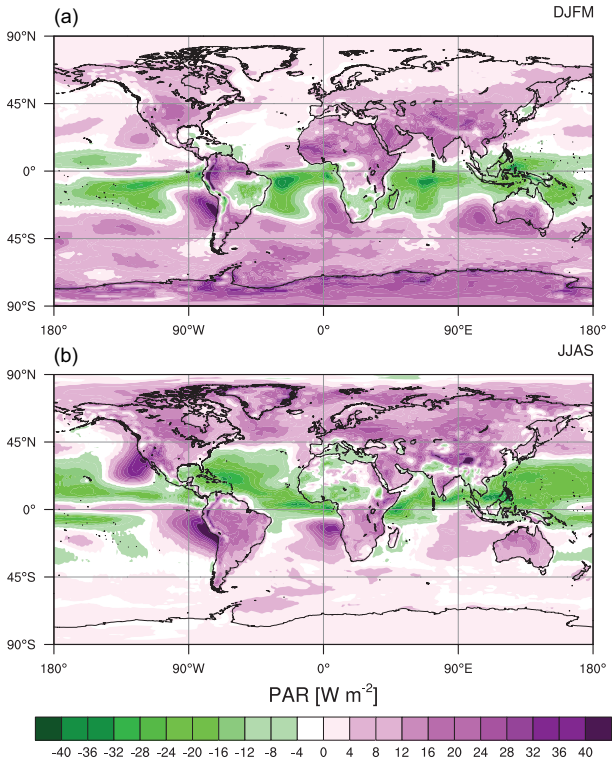

Figure 5. Biases in simulated photosynthetically available radiation (PAR) compared to the SRB satellite-derived observations (Pinker et al., 1992) averaged over 1986–2005. Winter **(a)** and summer **(b)** periods are computed from DJFM and JJAS months.

GMDD
8, 5671–5739, 2015

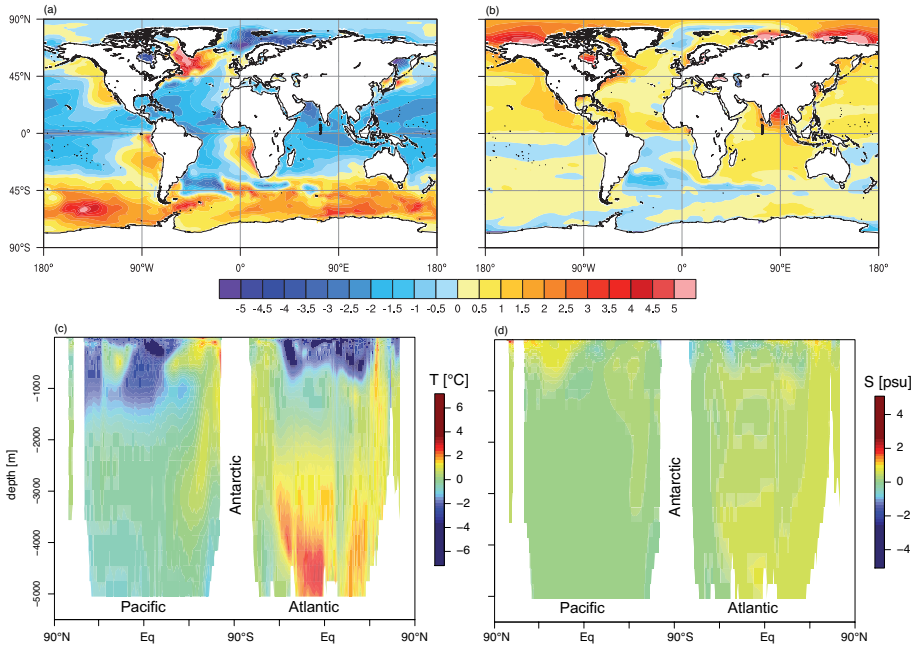

Figure 6. Annual bias patterns of simulated temperature *T* and salinity *S* averaged over 1986–2005 compared to the WOA2013 observations (Levitus et al., 2013). Surface biases for sea surface temperature **(a)** and salinity **(b)** are represented using the same colorbar. Vertical structure of biases for temperature **(c)** and salinity **(d)** are estimated using zonal-average biases from WOA2013 across the Atlantic and Pacific oceans.

GMDD
8, 5671–5739, 2015

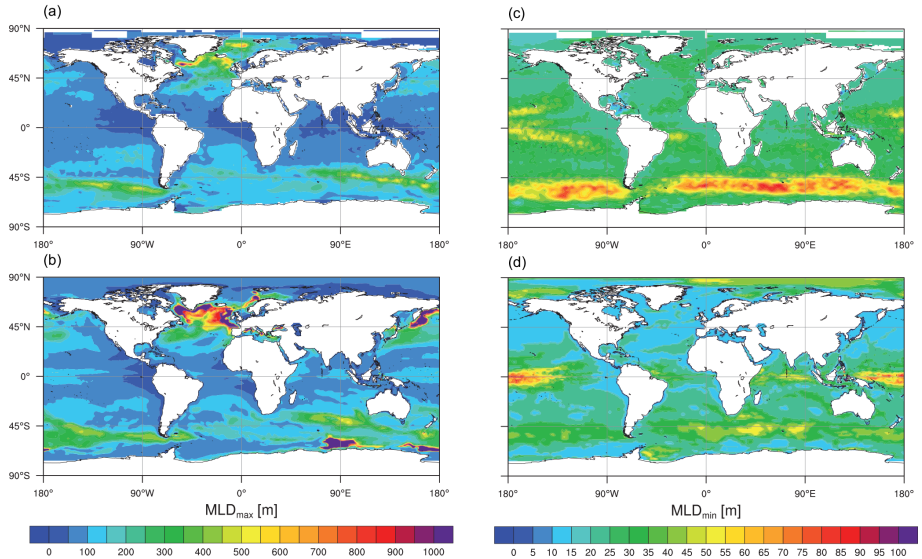

Figure 7. Composite of yearly extremum of mixed-layer depth over 1986–2005. Left panels represent the maximum mixed-layer depth (MLD_{max}) for **(a)** observations (Sallée et al., 2010) and **(b)** CNRM-ESM1. Right panels represent the minimum mixed-layer depth (MLD_{min}) for observations **(c)** and CNRM-ESM1 **(d)**.

GMDD
8, 5671–5739, 2015

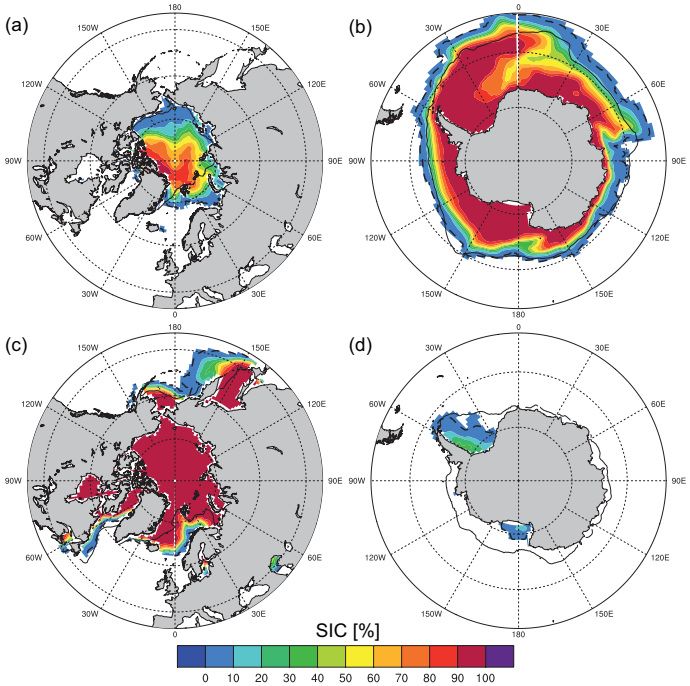

Figure 8. Sea ice cover (SIC) as simulated by CNRM-ESM1 averaged over 1986–2005. Top panels represent composite of September sea ice cover, while bottom panels are for March. Iso-15 % of SIC serves as comparison between model results and NSIDC observations (Cavalieri et al., 1996) averaged over 1986–2005; model results and observations are indicated with dashed and solid black lines, respectively.

GMDD
8, 5671–5739, 2015

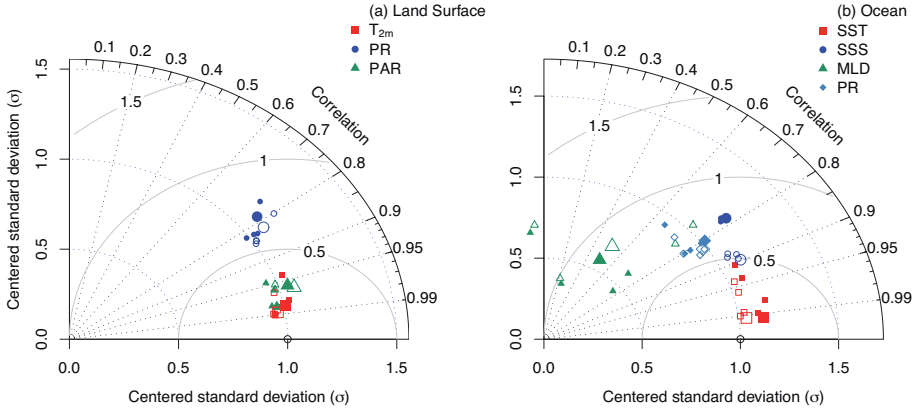

Figure 9. Taylor diagrams showing the correspondence between model results and observations for CNRM-ESM1 and CNRM-CM5.2. Near-surface temperature ($T_{2\,m}$), precipitation (PR) and incoming short-wave radiation (RSDS) are used to assess model performance over land surface. Sea surface temperature (SST), sea surface salinity (SSS), mixed-layer depth (MLD) and precipitation (PR) are used to assess model performance over ocean. Filled and empty symbols indicate skills for CNRM-ESM1 and CNRM-CM5.2, respectively. The size of the symbols indicates whether statistics were computed from annual mean climatology or seasonal average (JFM, AMJ, JAS, OND) over 1986–2005.

GMDD
8, 5671–5739, 2015

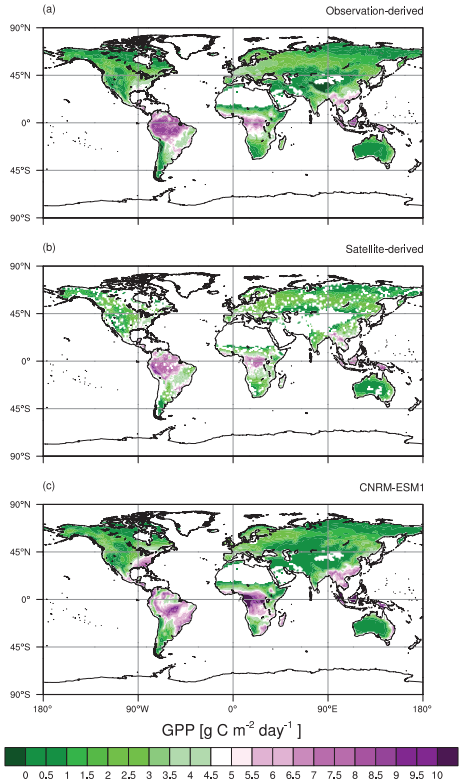

Figure 10. Annual-mean terrestrial gross primary production (GPP). Values are given for **(a)** observation-derived MTE-FluxNet (Jung et al., 2009) averaged over 1986–2005, **(b)** satellite-derived observation from MODIS over 2000–2013 and **(c)** CNRM-ESM1 over 1986–2005.

GMDD
8, 5671–5739, 2015

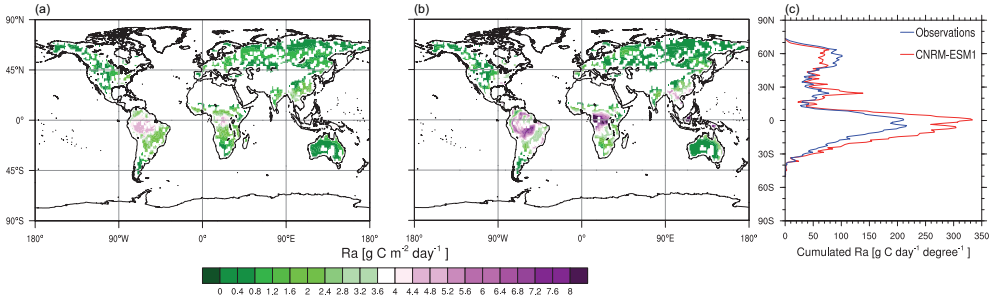

Figure 11. Annual-mean autotrophic respiration (Ra) as estimated from MODIS over 2000–2013 **(a)** and as simulated by CNRM-ESM1 **(b)** over 1986–2005. Panel **(c)** represents the zonal-cumulated Ra in function of latitude for both satellite-derived estimates (in blue) and CNRM-ESM1 (in red).

GMDD
8, 5671–5739, 2015

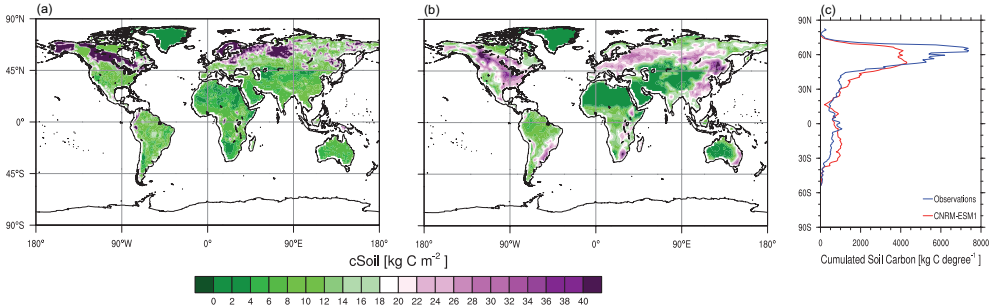

Figure 12. Stocks of modern soil organic carbon (cSoil) as estimated from FAO/IIASA/ISRIC/ISSCAS/JRC (2012) Harmonized World Soil Database **(a)** and as simulated by CNRM-ESM1 **(b)** averaged over 1986–2005. Panel **(c)** represents the zonally-cumulated soil organic stock in function of latitude for both observation-based estimates (in blue) and CNRM-ESM1 (in red).

GMDD
8, 5671–5739, 2015

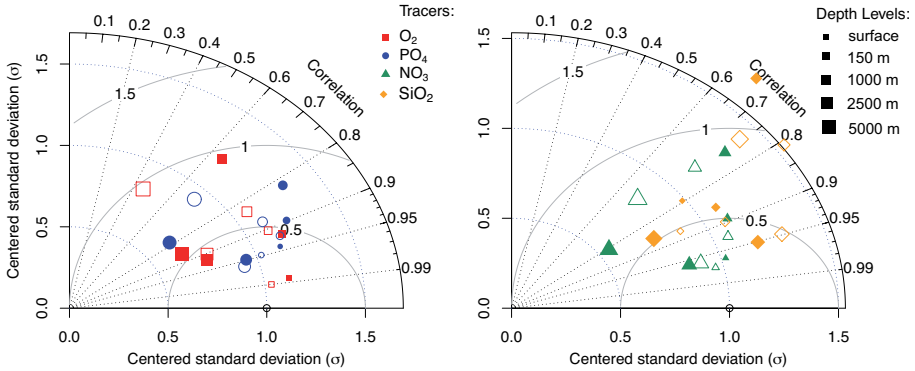

Figure 13. Taylor diagrams showing the correspondence between model results and observations for CNRM-ESM1 and CNRM-CM5.2 (Séférian et al., 2013). Climatological distribution over 1986–2005 of simulated Oxygen (O_2), phosphate (PO_4), nitrate (NO_3) and silicate (SiO_2) concentrations are assessed against WOA2013 data product. Filled and empty symbols indicate skills for CNRM-ESM1 and CNRM-CM5, respectively. The size of the symbols indicates the depth at which statistics have been computed.

GMDD
8, 5671–5739, 2015

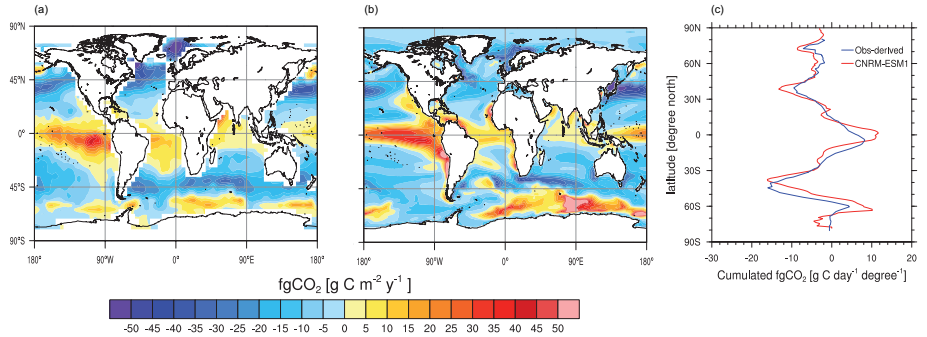

Figure 14. Annual-mean ocean carbon fluxes ($fgCO_2$) as estimated by the Takahashi et al. (2010) database **(a)** and as simulated by CNRM-ESM1 averaged over 1986–2005 **(b)**. Panel **(c)** represents the zonal-cumulated carbon fluxes in function of latitude for both observation-based estimates (in blue) and CNRM-ESM1 (in red). Negative (positive) fluxes indicate an uptake (outgasing) of CO_2.

GMDD
8, 5671–5739, 2015

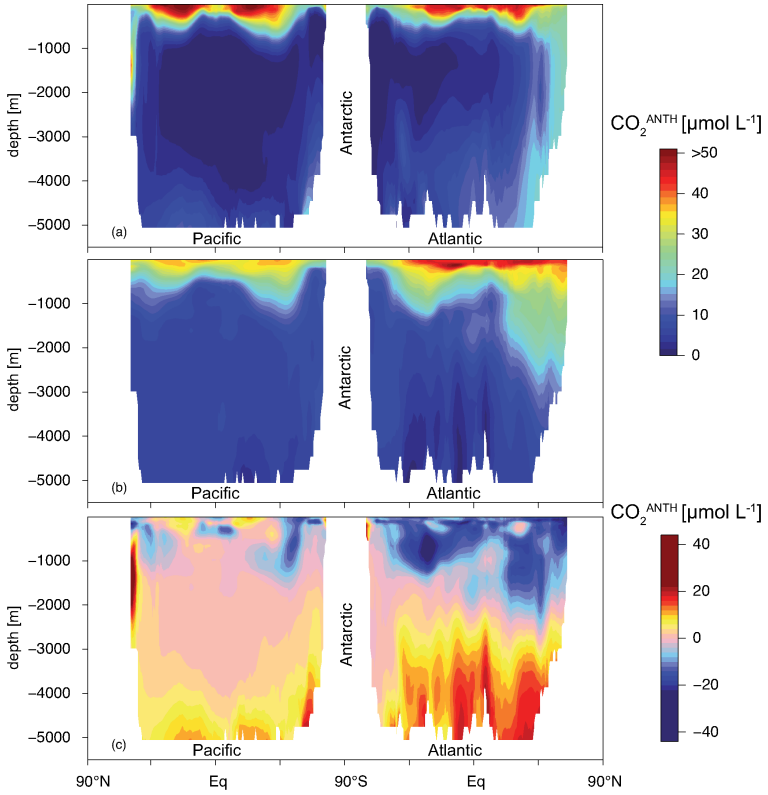

Figure 15. Annual-mean zonal-average anthropogenic carbon (CO_2^{ANTH}) across the Atlantic and Pacific oceans as simulated by CNRM-ESM1 averaged over 1990–2005 **(a)** and as estimated from the GLODAP database compiling data up to 1994 **(b)**. Panel **(c)** represents the mean-annual bias in zonal structures between model and observation-based estimates in CO_2^{ANTH}.

GMDD
8, 5671–5739, 2015

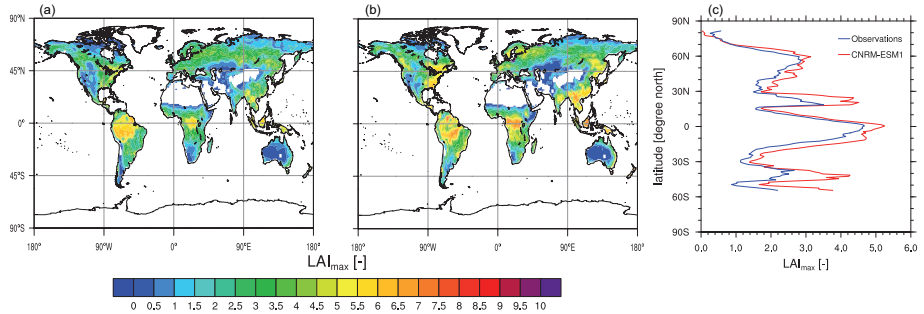

Figure 16. Composite of yearly maximum of leaf area index (LAI_{max}) as estimated from AVHRR satellite observations of Zhu et al. (2013) **(a)** and as simulated by CNRM-ESM1 **(b)** over 1986–2005. Panel **(c)** represents the zonal-average LAI_{max} in function of latitude for both observation-based estimates (in blue) and CNRM-ESM1 (in red).

GMDD
8, 5671–5739, 2015

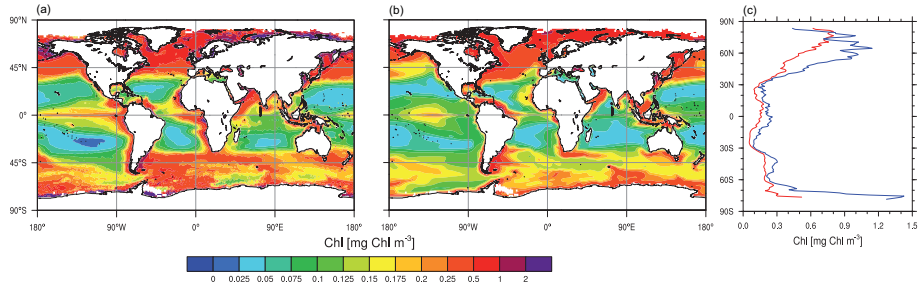

Figure 17. Annual-mean surface chlorophyll concentrations (Chl) as estimated from SeaWiFS over 1997–2010 **(a)** and as simulated by CNRM-ESM1 **(b)** over 1986–2005. Panel **(c)** represents the zonal-averaged Chl in function of latitude for both satellite-derived estimates (in blue) and CNRM-ESM1 (in red).

GMDD
8, 5671–5739, 2015

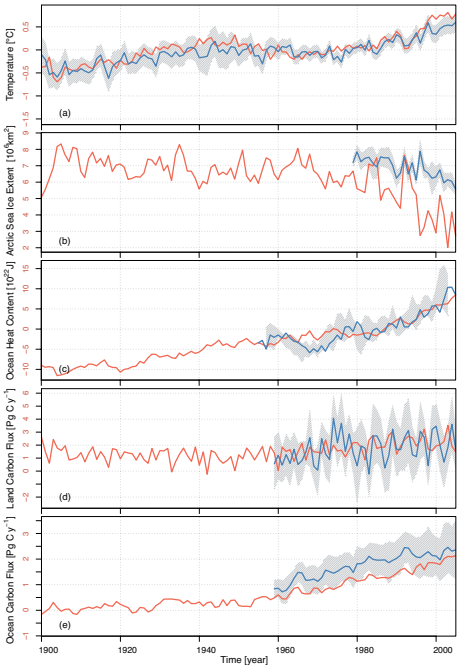

Figure 18. Time series of various climate indices as monitored from available observations (blue solid line) and as simulated by CNRM-ESM1 (red solid line) since 1901 with global near-surface temperature **(a)**, September arctic sea-ice extent **(b)**, 0–2000 m ocean heat content **(c)**, land carbon flux **(d)** and ocean carbon flux **(e)**. Hatching represents the $\pm 2\sigma$ estimated from the ensemble deviation between the 100 members of the HadCRUT4 database (Morice et al., 2012) for near-surface temperature, the standard deviation between NSIDC Fetterer et al. (2002), Comiso (1999) and Hadisst (Rayner et al., 2003) databases, the pentadal variability of the observed ocean heat content (Levitus et al., 2012) and spread between Global Carbon Project reconstructions for both land and ocean (Le Quéré et al., 2015). For both OCS and LCS, positive (negative) fluxes indicate an uptake (outgasing) of CO_2.

GMDD
8, 5671–5739, 2015